NASA Contractor Report 3645

The CMC:3DPNS Computer Program for Prediction of Three-Dimensional, Subsonic, Turbulent Aerodynamic Juncture Region Flow

Volume I - Theoretical

A. J. Baker

CONTRACT NAS1-15105
NOVEMBER 1982

NASA

NASA Contractor Report 3645

The CMC:3DPNS Computer Program for Prediction of Three-Dimensional, Subsonic, Turbulent Aerodynamic Juncture Region Flow

Volume I - Theoretical

A. J. Baker
Computational Mechanics Consultants, Inc.
Knoxville, Tennessee

Prepared for
Langley Research Center
under Contract NAS1-15105

National Aeronautics
and Space Administration

Scientific and Technical
Information Branch

1982

TABLE OF CONTENTS

SUMMARY

An order-of-magnitude analysis of the subsonic three-dimensional, steady time-averaged Navier-Stokes equations, for semi-bounded aerodynamic juncture geometries, yields the parabolic Navier-Stokes simplification. The numerical solution of the resultant pressure Poisson equation is cast into complementary and particular parts, yielding an iterative interaction algorithm with an exterior three-dimensional potential flow solution. A parabolic transverse momentum equation set is constructed, wherein robust enforcement of first-order continuity effects is accomplished using a penalty differential constraint concept within a finite element solution algorithm. A Reynolds stress constitutive equation, with low turbulence Reynolds number wall functions, is employed for closure, using parabolic forms of the two-equation turbulent kinetic energy-dissipation equation system. Numerical results document accuracy, convergence and utility of the developed finite element algorithm, and the CMC:3DPNS computer code applied to an idealized wing-body juncture region. Additional results document accuracy aspects of the algorithm turbulence closure model.

INTRODUCTION

A prime requirement in computational aerodynamics is flow prediction in juncture regions formed by the intersection of aerodynamic surfaces, e.g., wing-body, wing-winglet, pylon-wing, etc. In most instances of interest, the associated flow is three-dimensional, subsonic with variable density, and turbulent. The characteristic action of such flows is roll-up of a vortex in the plane transverse to the chord coordinate, and mass efflux/influx into the boundary layer regions located at some distance from the juncture region. The requirement of a numerical algorithm for the juncture flow is to predict the associated vortex structure, hence compute a corner drag coefficient, and to provide transverse plane velocity boundary conditions for a conventional three-dimensional boundary layer analysis of the associated farfield flows.

The essential key aspects of this problem are illustrated in the geometry of the idealized exterior subsonic axial corner, see Figure 1, which has received considerable theoretical and experimental attention. Rubin, et al., [1-4] pioneered in formulation and analysis of the three-dimensional laminar corner flow problem. Tokuda [5] documents an extension of this analysis, and compared his predictions to the experimental data of Zamir and Young [6]. Bragg [7] analyzed the corresponding turbulent flow case, and determined the corner distribution of the chordwise Reynolds normal stress component $\overline{u_1'u_1'}$. The salient feature of the turbulent flow case is inducement of a persistent axial vorticity component. Various causal mechanisms have been theorized, including transverse pressure waves [8], Reynolds shear stress gradients along the corner bisector [9], and nonisotropy of the Reynolds stress tensor [10]. Quality experimental data for a confined corner flow [11], compared to documentary results reported herein, indicate the primary mechanism to be nonisotropy of the Reynolds stress tensor $\overline{u_i'u_j'}$.

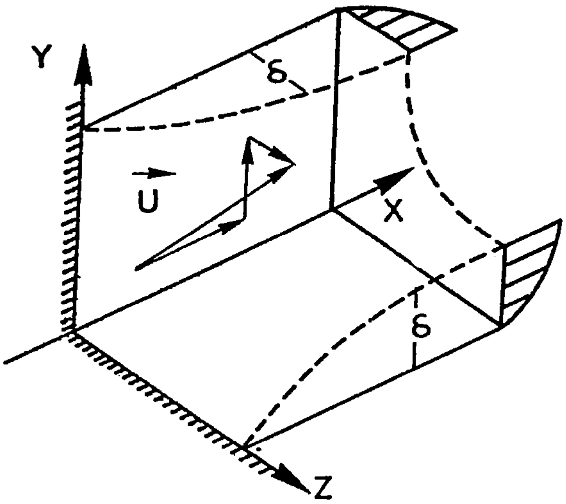

Figure 1.- Idealized Juncture Region Geometry

The character in the idealized corner region flow thus appears the result of a delicate balance between turbulence phenomena and the induced secondary mean flow velocity field. These mechanisms represent a balancing of higher-order effects however, as discussed herein, and can be readily dominated by flow-field curvature induced vorticity, cf. [12,13]. Nevertheless, an adequate Reynolds stress closure model is required and has been developed for this problem class. The six components of the (symmetric) Reynolds stress tensor are determined using a tensor field constitutive equation formulation which requires solution of parabolized forms of the transport equations for turbulent kinetic energy (k) and isotropic dissipation function (ε). The stress constitutive equation includes a low turbulence Reynolds number length scale model to permit solution of the (k, ε) equation system directly through the sublayer region adjacent to an aerodynamic surface. Hence, the boundary conditions for the k and ε solutions are identical vanishing at all aerodynamic surfaces.

A pressure-velocity formulation is undoubtedly preferred for an algorithm to predict turbulent aerodynamic juncture region flows. While definition of a transverse plane potential function [14] can automatically satisfy the continuity equation, the elimination of transverse pressure gradients comes at the expense of definition and use of vorticity. The acknowledged weakness of the vorticity formulation is the kinematic boundary condition statement. The existence of very large mean flow strain rates at an aerodynamic surface, for turbulent flow, serves to further complicate this intrinsic weakness. Conversely, in a physical variable formulation, an algorithm is required developed to construct an overall parabolic, i.e., initial-value, elliptic boundary value statement for transverse plane phenomena. A careful order of magnitude analysis of the transverse plane momentum equations indicates that pressure distributions will balance convection and/or turbulence effects to first order, and that overall, this balance is of higher order effects than controlled by the continuity equation. Since the continuity equation is not parabolic for subsonic flow, the construction of a suitable transverse plane equation system is required and presented.

The pressure-velocity formulation is derived and evaluated herein for steady turbulent flow prediction in three-dimensional,semi-bounded aerodynamic juncture region domains. Persistence of the chordwise component of the time-averaged, mean flow velocity permits an order of magnitude analysis, yielding the parabolic approximation to the governing three-dimensional, steady time-averaged Navier-Stokes equations. Using the same procedure for components of the Reynolds stress tensor, the balancing of lowest order terms in the two-transverse momentum equations yields a pressure Poisson equation. An algorithm for this equation is derived in terms of complementary and particular solution fields. The complementary solution is determined using boundary conditions obtained from an exterior potential flow solution. The particular solution refines this pressure determination by accounting for the Reynolds stress and transverse velocity distributions. The particular solution is enforced in a retarded manner in the chordwise momentum equation, to update the three-dimensional pressure field, yielding an iterative-interaction algorithm with the three-dimensional exterior potential flow solution. Algorithm convergence occurs when this composite pressure solution becomes stationary. As a consequence of the ordering analysis, the number of dependent variables requiring solution exceeds the available equations. Therefore, using finite element penalty function concepts in constrained extremization, cf. [15] , a transverse momentum equation solution statement is constructed wherein the first-order effects of the nonparabolic continuity equation are enforced as a differential constraint.

SYMBOLS

a	boundary condition coefficient
A	constant
b	constant
B	finite element two-dimensional hypermatrix prefix
C	turbulence model coefficient; initial-value matrix
E	energy norm
f	function of known argument
F	finite element matrix; discretized equation system
g	function of known argument
G	finite element matrix prefix
h	metric coefficient
H	stagnation enthalpy; Hilbert space
i	index
j	index
J	Jacobian matrix
k	turbulence kinetic energy; finite element basis degree
ℓ	summation index; differential operator
L	differential operator
M	number of finite elements spanning R^2
n	unit normal vector; dimension of space
N	finite element cardinal basis; discrete index
p	pressure; iteration index
q_j	heat flux vector; generalized dependent variable
Q_J	generalized semi-discrete dependent variable
R^2	spatial domain of differential operator
s,S	source term
S_e	finite element assembly operator
u_i	velocity vector
$\overline{u_i'u_j'}$	Reynolds kinematic stress tensor
U	convection matrix
x_i	Cartesian coordinate system
y^+	shear velocity Reynolds number
β_i	Lagrange multiplier set
∂	partial derivative operator
∂R	boundary of solution domain R^2
δ	Kronecker delta; parameter
δQ	iteration vector

Δ	mesh measure; increment
ε	isotropic dissipation function; parameter
η_i	curvilinear coordinate system
κ	heat conductivity coefficient
ν	kinematic viscosity
ρ	density
σ_{ij}	Stokes stress tensor
Σ	summation
ϕ	constraint dependent variable
ω	sublayer damping function
Ω	solution domain

Superscripts

e	finite element reference
h	solution approximation
o	initial condition reference
p	iteration index
T	matrix transpose
t	turbulent reference
$'$	ordinary derivative

Subscripts

e	finite element reference
i,j,k,ℓ	tensor indices
j	time step index
o	reference state

Notation

{ }	column matrix
[ ]	square matrix
$\sqcup$	union
$\sqcap$	intersection
ε	belongs to

PROBLEM DESCRIPTION

Parabolic Navier-Stokes Equations

The three-dimensional parabolic Navier-Stokes (3DPNS) equations are a simplification of the steady, three-dimensional time-averaged Navier-Stokes equations. In Cartesian tensor notation, and employing superscript tilde and bar to denote mass-weighted and conventional time-averaging respectively, [16], the conservative equation form for a variable density, heat conducting fluid is

$$L(\bar{\rho}) = \frac{\partial}{\partial x_j}\left[\bar{\rho}\tilde{u}_j\right] = 0 \tag{1}$$

$$L(\bar{\rho}\tilde{u}_i) = \frac{\partial}{\partial x_j}\left[\bar{\rho}\tilde{u}_i\tilde{u}_j + \bar{p}\delta_{ij} + \overline{\rho u_i' u_j'} - \bar{\sigma}_{ij}\right] = 0 \tag{2}$$

$$L(\bar{\rho}\tilde{H}) = \frac{\partial}{\partial x_j}\left[\bar{\rho}\tilde{H}\tilde{u}_j - \tilde{u}_i\bar{\sigma}_{ij} + \overline{\rho H' u_j'} - \overline{u_i'\sigma_{ij}'} + \bar{q}_j\right] = 0 \tag{3}$$

$$L(\bar{\rho}k) = \frac{\partial}{\partial x_j}\left[\bar{\rho}\tilde{u}_j k + \left(C_k\frac{k}{\varepsilon}\overline{\rho u_i' u_j'} - \bar{\mu}\delta_{ij}\right)\frac{\partial k}{\partial x_i}\right] + \overline{\rho u_i' u_j'}\,\frac{\partial \tilde{u}_i}{\partial x_j} + \bar{\rho}\varepsilon = 0 \tag{4}$$

$$L(\bar{\rho}\varepsilon) = \frac{\partial}{\partial x_j}\left[\bar{\rho}\tilde{u}_j\varepsilon + C_\varepsilon\frac{k}{\varepsilon}\overline{\rho u_i' u_j'}\frac{\partial \varepsilon}{\partial x_j}\right] + C_\varepsilon^1\,\overline{u_i' u_j'}\,\frac{\varepsilon\partial\tilde{u}_i}{k\partial x_j} + C_\varepsilon^2\frac{\bar{\rho}\varepsilon^2}{k} = 0 \tag{5}$$

In equations 1-3, $\bar{\rho}$ is density, $\tilde{u}_j$ is the mean velocity vector, $\bar{p}$ is pressure, δ_{ij} is the Kronecker delta, and $\tilde{H}$ is stagnation enthalpy. The Stokes stress tensor $\bar{\sigma}_{ij}$ and heat flux vector $\bar{q}_j$ are defined as,

$$\bar{\sigma}_{ij} = \bar{\rho}\bar{\nu}\,(\tilde{E}_{ij} - \frac{2}{3}\delta_{ij}\tilde{E}_{kk})\,/Re \tag{6}$$

$$\bar{q}_j = \bar{\kappa}\frac{\partial\tilde{H}}{\partial x_j} \tag{7}$$

where Re is the reference Reynolds number, Re = $U_\infty L/\nu_\infty$, and $-\rho\overline{u_i' u_j'}$ is the Reynolds stress tensor. In equations 6-7, $\bar{\nu}$ and $\bar{\kappa}$ are fluid kinematic viscosity and heat conductivity respectively, and $\tilde{E}_{ij}$ is the mean flow strain rate tensor

$$\tilde{E}_{ij} \equiv \frac{\partial \tilde{u}_i}{\partial x_j} + \frac{\partial \tilde{u}_j}{\partial x_i} \tag{8}$$

Equations 4-5 are the transport equations for turbulent kinetic energy and isotropic dissipation function, as obtained using the closure model of Launder, Reece and Rodi [17] for the pressure-strain and triple correlations, and

$$k \equiv \tfrac{1}{2}\overline{u_i' u_i'} \tag{9}$$

$$\varepsilon \equiv \frac{2\bar{\nu}}{3}\overline{\left[\frac{\partial u_i}{\partial x_j}\,\frac{\partial u_i}{\partial x_k}\right]}\delta_{jk} \tag{10}$$

The various coefficients C_β^α are model constants, cf. [18].

The parabolic Navier-Stokes equation set is derived from equations 1-5 by assuming the ratio of transverse mean velocity components to chordwise component is less than unity, and by further assuming that:

1. the chordwise velocity component suffers no reversal,
2. diffusive transport processes in the chordwise direction are higher-order, hence negligible, and
3. the overall elliptic character of the parent three-dimensional Navier-Stokes equation is enforcable through construction of a suitable pressure field with exterior flow boundary conditions.

Assume the x_1 (curvilinear) coordinate direction parallel to the chordwise mean flow direction, with scalar velocity component $\tilde{u}_1$ of order unity, i.e. O(1). Further assume $O(\tilde{u}_2) \sim O(\delta) \approx O(\tilde{u}_3)$, and that $O(\delta) < O(1)$. As occurs with boundary layer theory, the continuity equation confirms that chordwise variation in $\tilde{u}_1$ is of the order equal to appropriate transverse variation of $\tilde{u}_2$ and $\tilde{u}_3$; hence, for $\frac{\partial}{\partial x_1} \approx O(1)$, $\frac{\partial}{\partial x_2} \approx O(\delta^{-1}) \approx \frac{\partial}{\partial x_3}$.

Determination of the relative order of terms in the momentum equation 2 is straightforward. For the $\tilde{u}_1$ equation, since $O(\overline{\rho u_i' u_j'})$ must be $O(\delta)$, the term $\frac{\partial}{\partial x_1}(\overline{\rho u_1' u_1'})$ is higher order and can be discarded. The assumption that chordwise diffusion is negligible infers that $\frac{\partial}{\partial x_1}(\tilde{E}_{11}) \approx 0$, hence $O(Re^{-1}) \leq O(\delta)$. Therefore, the terms in $\bar{\sigma}_{12}$ and $\bar{\sigma}_{13}$ involving $\tilde{u}_2$ and $\tilde{u}_3$ i.e., $\frac{\partial}{\partial x_2}\left(\frac{\partial \tilde{u}_2}{\partial x_1}\right)$ and $\frac{\partial}{\partial x_3}\left(\frac{\partial \tilde{u}_3}{\partial x_1}\right)$, are both $O(\delta)$ or smaller and can be neglected.

Deletion of these terms is fundamental to the parabolic approximation, since their elimination removes the elliptic boundary value character in the chordwise flow direction. The existence of $\frac{\partial}{\partial x_1}(\bar{\rho}\tilde{u}_1\tilde{u}_1)$ instills an initial value character in the resultant equation, hence, permits marching the solution for $\tilde{u}_1$ in the chordwise direction. The desired 3DPNS form, denoted $L^p(\cdot)$, is therefore,

$$L^p(\bar{\rho}\tilde{u}_1) \equiv \frac{\partial}{\partial x_1}(\bar{\rho}\tilde{u}_1\tilde{u}_1) + \frac{\partial \bar{p}}{\partial x_1} + \frac{\partial}{\partial x_2}\left[\overline{\rho u_1' u_2'} - \bar{\sigma}_{12}\right]$$

$$+ \frac{\partial}{\partial x_3}\left[\overline{\rho u_1' u_3'} - \bar{\sigma}_{13}\right] = 0 \qquad (11)$$

which is thoroughly familiar. As a final note, should x_j correspond to a curvilinear coordinate description, the derivatives expressed in equation 11 are interpreted as covariant derivatives. The 3DPNS form of the energy equation (3), similarly constructed, is

$$L^p(\bar{\rho}\tilde{H}) = \frac{\partial}{\partial x_1}(\bar{\rho}\tilde{u}_1\tilde{H}) + \frac{\partial}{\partial x_\ell}\left[\bar{\rho}\tilde{H}\tilde{u}_\ell - \tilde{u}_i\bar{\sigma}_{i\ell} + \overline{\rho H' u_\ell'} - \overline{u_i'\sigma_{i\ell}'} + \bar{q}_\ell\right] = 0 \qquad (12)$$

Equation 12 introduces the 3DPNS limited index summation convention $1 \leq (i,j) \leq 3$ and $2 \leq \ell \leq 3$.

In agreement with boundary layer concepts, the order of pressure variation in the transverse plane is assumed controlled by the lowest order terms appearing in equation 2 written on $\tilde{u}_2$ and $\tilde{u}_3$. Each transverse derivative of $\overline{\rho u_2' u_j'}$ and $\overline{\rho u_3' u_j'}$ is $O(1)$, while all other terms are $O(\delta)$ and higher. Thus, for a conventional two-dimensional boundary layer flow, for example,

$$L^p(\bar{\rho}\tilde{u}_2) \approx \frac{\partial}{\partial x_2}\left[\bar{p} + \overline{\rho u_2' u_2'}\right] = 0 \qquad (13)$$

The solution is trivial; $\bar{p}$ differs from the inviscid flow edge pressure by a constant, equal to a fraction of the free-stream turbulence (k) level, and is distributed through the boundary layer in proportion to $\overline{\rho u_2' u_2'}$. The initial value character for pressure, as exhibited by the 3DPNS first order approximation to equation 2, for $\tilde{u}_2$ and $\tilde{u}_3$, is recast into a more tractable form by taking the divergence. Retaining the higher-order convection and diffusion terms for generality, the consistent 3DPNS form for both transverse momentum equations is

$$L(\bar{p}) = \frac{\partial^2 \bar{p}}{\partial x_\ell^2} + \frac{\partial^2}{\partial x_j \partial x_\ell}\left[\bar{\rho}\tilde{u}_\ell \tilde{u}_j + \overline{\bar{\rho} u_\ell' u_j'} - \bar{\sigma}_{\ell j}\right] = 0 \tag{14}$$

Equation 14 defines an elliptic boundary value problem for determination of pressure distribution in the transverse plane. The pressure field that satisfies this quasi-linear Poisson equation consists of complementary and particular solutions, i.e.,

$$\bar{p}(x_i) = p_c(x_i) + p_p(x_i) \tag{15}$$

The complementary solution satisfies the homogeneous form of equation 14, i.e.,

$$L^p(p_c) = \frac{\partial^2 p_c}{\partial x_\ell^2} = 0 \tag{16}$$

The Dirichlet boundary condition for equation 16 is $p_c(x_1, \bar{x}_\ell) \equiv \bar{p}(x_1, \bar{x}_\ell)$, on the intersection of the 3DPNS domain with the exterior potential flow domain. Elsewhere, the boundary condition for p_c is homogeneous Neumann.

The particular pressure is any solution to equation 14 subject to homogeneous Dirichlet boundary conditions on boundary segments where p_c is known. Elsewhere, the nonhomogeneous Neumann constraint is provided by the inner product of the 3DPNS form of equation 2, written on $\tilde{u}_\ell$, with the local outward pointing unit normal $\hat{n}_\ell$.

$$\ell(p_p) \equiv L^p(\bar{\rho}\tilde{u}_i)\cdot\hat{n}_\ell = \frac{\partial}{\partial x_\ell}\left[p_p + \rho\overline{u_\ell' u_\ell'}\right] + \frac{\partial}{\partial x_k}\left[\rho\overline{u_k' u_\ell'}\right] = 0 \tag{17}$$

Repeated indices in equation 17 are not summed, and $2 \leq k \leq 3$ for $k \neq \ell$. Hence,equation 17 is the generalization of the boundary layer form, equation 13. Following determination of the order of terms in the Reynolds stress tensor in the next section, the nonhomogeneous terms in equation 17 vanish to lowest order on an aerodynamic surface. Hence, thereupon $p_p(x_1, \bar{x}_\ell)$ is a constant which is zero. Elsewhere on the 3DPNS domain boundary, equation 17 yields the appropriate boundary condition for equation 14.

Reynolds Stress Tensor Closure

A closure expression for the kinematic Reynolds stress tensor $-\overline{u_i'u_j'}$, appearing in equations 4-5, is required to complete the 3DPNS order of magnitude analysis. The necessary insight is provided by construction of a tensor field strain-rate constitutive equation, the existence of which is assured at "sufficient" distance from boundaries in space and time [19]. Using lower-dimensional order of magnitude analyses and invariance, the three lead terms of the five term expansion of the kinematic form, appropriate for 3DPNS analyses , are [20],

$$-\overline{u_i'u_j'} = -k\alpha_{ij} + C_4\frac{k^2}{\varepsilon}\tilde{E}_{ij} + C_2C_4\frac{k^3}{\varepsilon^2}\tilde{E}_{ik}\tilde{E}_{kj} + \cdots \tag{18}$$

$\tilde{E}_{ij}$ is the symmetric mean flow strain-rate tensor, equation 8, and k and ε are turbulence parameters defined in equations 9-10.

Equation 18 results from re-expression of the triple correlations, within the Reynolds stress transport equation, using the model of Launder, Reece and Rodi [17] , and is the tensor generalization of the original analysis by Gessner and Emery [10]. In equation 18, α_{ij} is a diagonal tensor in the principal coordinates, defined as

$$\alpha_{ij} \equiv \frac{1}{3k}\left(\overline{u_k'u_k'}\right)a_{\underline{i}}\delta_{ij} \tag{19}$$

The $a_{\underline{i}}$ are coefficients admitting anisotropy, where $a_1 \equiv C_1$, and $a_2 \equiv C_3 \equiv a_3$. The $C_{\underline{\alpha}}$ are defined [17] as

$$C_1 \equiv \frac{22(C_{01} - 1) - 6(4C_{02} - 5)}{33(C_{01} - 2C_{02})}$$

$$C_2 \equiv \frac{4(3C_{02} - 1)}{11(C_{01} - 2C_{02})}$$

$$C_3 \equiv \frac{22(C_{01} - 1) - 12(3C_{02} - 1)}{33(C_{01} - 2C_{02})}$$

$$C_4 \equiv \frac{44C_{02} - 22C_{01}C_{02} - 128C_{02} - 36C_{02}^2 + 10}{165(C_{01} - 2C_{02})^2} \qquad \textbf{(20)}$$

In equation 20, C_{01} and C_{02} are "universal" empirical constants; suggested values are $C_{01} \approx 2.8$ and $C_{02} \approx 0.45$, [18].

The order of terms in equation 18 can be estimated for the standard values $C_\alpha = \{0.94, 0.067, 0.56, 0.068\}$. For significance in equation 2, recall $O(\overline{u_i'u_j'}) = O(\delta)$. For a two-dimensional flow, and for i = 1 and j = 2, equation 18 yields the familiar form

$$-\overline{u_1'u_2'} = C_4 \frac{k^2}{\varepsilon} \frac{\partial \tilde{u}_1}{\partial x_2} \qquad (21)$$

Hence, $O(C_4 k^2/\varepsilon) = O(\delta^2)$. Further for $i = 1 = j$, and neglecting the second two terms, $O(k) = O(\delta)$, hence $O(C_4/\varepsilon) = O(1)$. To proceed further requires an estimate of the magnitude of $O(k)$. For a steady, subsonic, turbulent aerodynamic flow, away from the influence of the wall or freestream, the magnitude of the fluctuating component of velocity will probably not exceed about 10% of the steady component. Hence, equation 9 in nondimensional form yields the estimate $O(k) \leq O(10^{-2})$. Taking the maximum yields $O(\delta) \leq O(10^{-2})$; evaluating the fourth term of equation 20 and comparing yields $O(C_4) \approx O(\delta^{\frac{1}{2}})$, hence $O(\varepsilon) \approx O(\delta^{\frac{1}{2}})$. Thus, $O(C_2 C_4 \frac{k^3}{\varepsilon^2}) \approx O(\delta^2)$. Therefore, in rectangular Cartesian coordinates, and retaining terms of the first two orders of significance, the six components of the kinematic Reynolds stress tensor for a 3DPNS analysis are

$$
\begin{array}{lll}
 & \overbrace{\hspace{7cm}}^{O(\delta)} & \overbrace{\hspace{6cm}}^{O(\delta^2)} \\
\overline{u_1'u_1'} = & C_1 k - C_2C_4\frac{k^3}{\varepsilon^2}\left[\left(\frac{\partial\tilde{u}_1}{\partial x_2}\right)^2 + \left(\frac{\partial\tilde{u}_1}{\partial x_3}\right)^2\right] & - 2C_4\frac{k^2}{\varepsilon}\left[\frac{\partial\tilde{u}_1}{\partial x_1}\right] \\
\overline{u_2'u_2'} = & C_3 k - C_2C_4\frac{k^3}{\varepsilon^2}\left[\frac{\partial\tilde{u}_1}{\partial x_2}\right]^2 & - 2C_4\frac{k^2}{\varepsilon}\left[\frac{\partial\tilde{u}_2}{\partial x_2}\right] \\
\overline{u_3'u_3'} = & C_3 k - C_2C_4\frac{k^3}{\varepsilon^2}\left[\frac{\partial\tilde{u}_1}{\partial x_3}\right]^2 & - 2C_4\frac{k^2}{\varepsilon}\left[\frac{\partial\tilde{u}_3}{\partial x_3}\right] \\
\overline{u_1'u_2'} = & \qquad - C_4\frac{k^2}{\varepsilon}\left[\frac{\partial\tilde{u}_1}{\partial x_2}\right] & - C_2C_4\frac{k^3}{\varepsilon^2}\left[\frac{\partial\tilde{u}_1}{\partial x_3}\left(\frac{\partial\tilde{u}_2}{\partial x_3} + \frac{\partial\tilde{u}_3}{\partial x_2}\right)\right. \\
 & & \left. + 2\frac{\partial\tilde{u}_1}{\partial x_2}\left(\frac{\partial\tilde{u}_1}{\partial x_1} + \frac{\partial\tilde{u}_2}{\partial x_2}\right)\right] \\
\overline{u_1'u_3'} = & \qquad - C_4\frac{k^2}{\varepsilon}\left[\frac{\partial\tilde{u}_1}{\partial x_3}\right] & - C_2C_4\frac{k^3}{\varepsilon^2}\left[\frac{\partial\tilde{u}_1}{\partial x_2}\left(\frac{\partial\tilde{u}_2}{\partial x_3} + \frac{\partial\tilde{u}_3}{\partial x_2}\right)\right. \\
 & & \left. + 2\frac{\partial\tilde{u}_1}{\partial x_3}\left(\frac{\partial\tilde{u}_1}{\partial x_1} + \frac{\partial\tilde{u}_3}{\partial x_3}\right)\right] \\
\overline{u_2'u_3'} = & \qquad - C_2C_4\frac{k^3}{\varepsilon^2}\left[\frac{\partial\tilde{u}_1}{\partial x_2}\,\frac{\partial\tilde{u}_1}{\partial x_3}\right] & - C_4\frac{k^2}{\varepsilon}\left[\frac{\partial\tilde{u}_2}{\partial x_3} + \frac{\partial\tilde{u}_3}{\partial x_2}\right]
\end{array}
\tag{22}
$$

Two conclusions regarding equation 22 should be noted. The terms which would provide an elliptic boundary value definition in the x_2, x_3 plane, for direct integration of equations 2, for $\tilde{u}_2$ and $\tilde{u}_3$, cf. [21], are indeed $O(\delta^2)$, in agreement with the ordering arguments leading to equation 14. Secondly, the $O(\delta)$ term in $-\overline{u_2'u_3'}$ in equation 22 vanishes on an aerodynamic surface, hence thereupon p_p is a constant. With this development, the order of terms in equations 4-5 can be determined, yielding the appropriate 3DPNS approximation as,

$$
\begin{aligned}
L^P(k) = \frac{\partial}{\partial x_i}(\bar{\rho}\tilde{u}_i k) &+ \frac{\partial}{\partial x_i}\left[\bar{\rho}\left(C_k\frac{k}{\varepsilon}\overline{u_i'u_\ell'} - \bar{\nu}\right)\frac{\partial k}{\partial x_\ell}\right] \\
&+ \bar{\rho}\;\overline{u_1'u_\ell'}\frac{\partial\tilde{u}_1}{\partial x_\ell} + \bar{\rho}\varepsilon = 0
\end{aligned}
\tag{23}
$$

$$L^p(\varepsilon) = \frac{\partial}{\partial x_i}(\rho\tilde{u}_i\varepsilon) + \frac{\partial}{\partial x_i}\left[C_{\varepsilon}\frac{k}{\varepsilon}\overline{u_i'u_\ell'}\,\frac{\partial\varepsilon}{\partial x_\ell}\right]$$

$$C_\varepsilon^1\ \overline{\rho u_1'u_\ell'}\,\frac{\varepsilon}{k}\frac{\partial\tilde{u}_1}{\partial x_\ell} + C_\varepsilon^2\ \bar{\rho}\,\frac{\varepsilon^2}{k} = 0 \tag{24}$$

recalling the 3DPNS limited summation convention, $1 \leq i \leq 3$, $2 \leq \ell \leq 3$.

Definition of boundary conditions for equations 23-24 requires addressing the issue of what constitutes "sufficient" distance for validity of equation 18. For two-dimensional flows, one approach is to employ similarity arguments to assign values to k and ε at some distance from the wall, e.g. $10 < y^+ < 50$, where $y^+ \equiv \frac{u_\tau x_2}{\bar{\nu}}$ is a turbulence Reynolds number based on wall shear velocity $u_\tau \equiv \sqrt{\tau_w/\bar{\rho}}$, see [16]. Extension of this concept to three-dimensional flows is questionable, but has been attempted [21]. A second alternative [22] suggests modifying the "constants" C_β^α appearing in equations 23-24, and integrating directly through the low turbulence wall region with $k \equiv 0 \equiv \varepsilon$ as boundary conditions.

The alternative approach of [23] is employed for the juncture region analysis. The "constants" C_α of the Reynolds stress constitutive equation 18 are modified to account for low turbulence levels in the sublayer region. Equation 21 defines the conventional turbulent "eddy viscosity" $\nu^t \equiv C_4k^2/\varepsilon$. Using dimensional analysis, ν^t is the product of a scale velocity and a scale length; typically, for a turbulence kinetic energy model,

$$\nu^t \equiv k^{\frac{1}{2}}\ell_d \tag{25}$$

Comparison with equation 21 yields the familiar relationship

$$\ell_d \equiv C_4\,\frac{k^{3/2}}{\varepsilon} \tag{26}$$

Recalling the van Driest damping function ω, defined to control evolution of the Prandtl mixing length scale [16], equation 26 multiplied by ω yields equation 21 in the form

$$-\overline{u_1'u_2'} = \omega\ C_4\frac{k^2}{\varepsilon}\ \frac{\partial\tilde{u}_1}{\partial x_2} \tag{27}$$

The conventional form [16] for ω is modified, for variable length scale damping, as

$$\omega \equiv \left[1 - \exp(-by^{+}/A^{+})\right] \tag{28}$$

where $A^{+} \approx 26$, and $b \approx 2.0$ based upon results of numerical studies [23, 24]. Therefore, premultiplying each of the coefficients C_{α} in equation 20 by ω produces the required sublayer modification for equation 18. Furthermore, C_{ε}^{2} in equation 24 is also multiplied by ω. The aerodynamic surface boundary conditions for equations 23-24 are then $k \equiv 0 \equiv \varepsilon$.

Differential Equation System Closure

Development of the lowest order parabolic Navier-Stokes differential equation system, as a subset of the steady, time-averaged Navier-Stokes system is complete. This 3DPNS system, equations 11, 12, 14, 18, 23 and 24, numbers one less than the number of dependent variables defined in equations 1-10. Therefore, at least one equation governing $O(\delta)$ phenomena must be included to close the system. Since the 3DPNS momentum equation 11 is written on $\tilde{u}_1$ only, both components of $\tilde{u}_{\ell} \equiv \{\tilde{u}_2, \tilde{u}_3\}$ are required determined subject to the constraint of continuity, equation 1. The finite element algorithm accomplishes this by "penalizing" the solution of the $O(\delta)$ 3DPNS approximation to the momentum equations 2, written on both components of $\tilde{u}_{\ell}$, by the continuity equation (error). Retaining the first two orders of terms, the 3DPNS form for the transverse momentum equations is,

$$\begin{aligned} L^{P}(\rho\tilde{u}_k) = {} & \frac{\partial}{\partial x_1}\left[\bar{\rho}\tilde{u}_1\tilde{u}_k + \overline{\rho u_1' u_k'}\right] \\ & + \frac{\partial}{\partial x_{\ell}}\left[\bar{\rho}\tilde{u}_{\ell}\tilde{u}_k + \overline{\rho u_{\ell}' u_k'} + \bar{p}\delta_{k\ell} - \bar{\sigma}_{k\ell}\right] = 0 \end{aligned} \tag{29}$$

which introduces the additional 3DPNS limited index $2 \leq k \leq 3$. The middle two terms in the second bracket are $O(\delta)$, while the remaining terms are all $O(\delta^2)$ or smaller. Equation 29 exhibits elliptic boundary value character in the x_2, x_3 plane, retaining the terms of $O(\delta^2)$ in the Reynolds stress tensor, equation 18, and contains the initial-value term permitting chordwise marching.

Since equation 29 represents two additional scalar equations, an auxillary dependent variable is required defined. The theoretical concept, borrowed from the variational calculus, is to define a suitable measure of the continuity equation (error), which is then applied as a differential constraint on solution of the transverse momentum equation 29. This constraint measure must span the transverse plane R^2, and must vanish as the continuity equation 1 becomes satisfied. Based on computational experience [23], an appropriate dependent variable is the harmonic function $\phi(x_\ell)$, defined as the solution to the Poisson equation

$$L^P(\phi) \equiv \frac{\partial^2\phi}{\partial x_\ell^2} - \frac{\partial}{\partial x_i}(\bar{\rho}\tilde{u}_i) \equiv 0 \qquad (30)$$

subject to homogeneous Neumann boundary conditions on portions of the domain boundary ∂R, and setting $\phi = 0$ at one location at least on ∂R. Equation 30 becomes homogeneous, as the continuity equation becomes satisfied, and the solution $\phi(x_\ell)$ becomes null as a consequence of the boundary condition specifications.

Grid Stretching Transformation

An elementary grid stretching coordinate transformation is of potential use for the general problem class, and is consistent with the ordering simplifications yielding the 3DPNS equation system. The transformation $\eta_i = \eta_i(x_j)$ that normalizes transverse spans with boundaries $f_{\ell i}$, $2 \le \ell \le 3$, $1 \le i \le 2$, is

$$\{\eta_i\} \equiv \left\{ \begin{array}{c} x_1 \\ \dfrac{x_2 - f_{21}(x_1)}{[f_{22}(x_1) - f_{21}(x_1)]/f_2} \\ \dfrac{x_3 - f_{31}(x_1)}{[f_{32}(x_1) - f_{31}(x_1)]/f_3} \end{array} \right\} \qquad (31)$$

The $f_{\ell i}(x_1)$ are piecewise continuous segments defining the transverse plane boundary ∂R of R^2, and the f_ℓ are normalizing coefficients. Using the chain rule, differentiation on x_1 introduces additional derivatives on η_ℓ. In particular,

$$\frac{\partial}{\partial x_1} = \frac{\partial}{\partial \eta_1} - [h_{22} + \eta_2 h_{23}] \frac{\partial}{\partial \eta_2} - [h_{32} + \eta_3 h_{33}] \frac{\partial}{\partial \eta_3}$$

$$\frac{\partial}{\partial x_2} = h_{21} \frac{\partial}{\partial \eta_2}$$

$$\frac{\partial}{\partial x_3} = h_{31} \frac{\partial}{\partial \eta_3} \qquad (32)$$

The functions $h_{\ell i}$, $1 \leq i \leq 3$, are defined as

$$\{h_{\ell i}\} \equiv \left\{ \begin{array}{l} f_\ell (f_{\ell 2} - f_{\ell 1})^{-1} \\ h_{\ell 1} f'_{\ell 1} \\ h_{\ell 1} f_\ell^{-1} \, (f'_{\ell 2} - f'_{\ell 1}) \end{array} \right\} \qquad (33)$$

The superscript prime denotes the (ordinary) derivative with respect to x_1, and the η_i coordinate system is fixed in the transform space.

FINITE ELEMENT SOLUTION ALGORITHM

The consistently ordered 3DPNS equation system has been constructed for the dependent variable set $q_j(x_i) \equiv \{q\} = \{\bar{\rho}, \tilde{u}_1, \tilde{u}_2, \tilde{u}_3, \tilde{H}, \bar{p}, k, \varepsilon, \overline{u_i' u_j'}, \phi\}^T$. An equation of state $\bar{\rho} = \bar{\rho}(\bar{p}, \tilde{H})$ closes the system. Equations 11, 12, 23, 24, and 29 of the 3DPNS equation set contain the initial-value term that facilitates solution marching in the chordwise direction. Equations 14 and 30 are elliptic boundary value descriptions with parametric initial-value dependence, while equation 18 is a local constitutive definition. Equation 1 becomes recast as the differential constraint using equation 30.

The general form of 3DPNS system description is

$$L^P(q_j) = \frac{\partial}{\partial x_1}(\bar{\rho}\tilde{u}_1 q_j) + \frac{\partial}{\partial x_\ell}\left[\rho\tilde{u}_\ell q_j + g_{\ell j}\right] + s_j = 0 \tag{34}$$

For equation 34, $g_{\ell j}$ and s_j are specified non-linear functions of their arguments, as determined by the index j. The three-dimensional partial differential equation 34 is defined on the Euclidian space R^3 spanned by the $x_i(\eta_i)$ coordinate system. The solution domain Ω is defined as the product of R^2 and x_1, for all elements of x_1 belonging to the open interval measured from $x_1(0)$, i.e.,

$$\Omega \equiv R^2 \times x_1 = \{(x_\ell, x_1): x_\ell \varepsilon R^2 \text{ and } x_1 \varepsilon [x_1(0), x_1)\}$$

The boundary $\partial\Omega$ of the solution domain is the product of the boundary ∂R of R^2 and x_1, i.e., $\partial\Omega \equiv \partial R \times x_1$. Thereupon, a differential constraint is applied of the form

$$\ell(q_j) = a_1 q_j + a_2 \frac{\partial}{\partial x_i} q_j \hat{n}_i + a_3 = 0 \tag{35}$$

In equation 35, the a_i are specified coefficients and $\hat{n}_i$ is the outwards pointing unit normal vector. Finally, an initial distribution for the appropriate members of q_j on $\Omega_0 \equiv R^2 \times x_1(0)$ is required.

$$q_j(x_\ell, x_1) \equiv q_j^0(x_\ell) \tag{36}$$

For the finite element numerical solution algorithm of equations 34-35, the approximation $q_j^h(x_\ell, x_1)$ to the (unknown) exact solution $q_j(x_\ell, x_1)$ is constructed from members of a finite-dimensional subspace of $H_0^1(\Omega)$, the Hilbert space of all functions possessing square integrable first derivatives and satisfying the boundary condition 35. While extremely flexible in theory, the practice for the 3DPNS equation system is to employ linear polynomials, defined on disjoint interior triangular-shaped subdomains R_e^2, the union of which forms the discretization of R^2. Hence, the finite element approximation is

$$q_j(x_\ell,x_1) \approx q_j^h(x_\ell,x_1) \equiv \sum_{e=1}^{M} q_j^e(x_\ell,x_1) \tag{37}$$

using the elemental construction

$$q_j^e(x_\ell,x_1) \equiv \{N_1(x_\ell)\}^T\{QJ(x_1)\}_e \tag{38}$$

In equations 37-38, j is a free index denoting members of $\{q^h\}$, and subscript or superscript e denotes pertaining to the $e^{\underline{th}}$ finite element, $\Omega_e \equiv R_e^2 \times x_1$. The elements of the row matrix $\{N_1(x_\ell)\}^T$ are linear polynomials on x_ℓ, $2 \leq \ell \leq 3$, [28], and elements of $\{QJ\}_e$ are the values of q_j^e at the nodes of R_e^2 .

The functional requirement of any numerical solution algorithm is to render the error in q_j^h minimum in some norm. The finite element algorithm requires the error in equations 34 and 35, i.e., $L^P(q_j^h)$ and $\ell(q_j^h)$, to be orthogonal to the space $\{N_1(x_\ell)\}$ employed to define q_j^h. In addition, the discrete approximation $L^p(\bar{\rho}^h)$ to the continuity equation 1 must be enforced as a differential constraint. Identifying the (Lagrange) multiplier set β_i, these linearly independent constraints are combined to yield the finite element solution algorithm theoretical statement.

$$\int_{R^2}\{N_k\}L^P(q_j^h)d\vec{x} + \beta_1\int_{\partial R}\{N_k\}\ell(q_j^h)d\vec{x} + \vec{\beta}_2\cdot\int_{R^2}\nabla\{N_k\}L^P(\bar{\rho}^h)d\vec{x} \equiv \{0\} \tag{39}$$

Equation 39 represents a system of ordinary differential equations, written on the chordwise coordinate x_1, of the form

$$[C]\{QJ\}' + [U]\{QJ\} + [GLJ]\{QL\} + \{SJ\} = \{0\} \tag{40}$$

A one-to-one correspondence of terms in equations 40 and 34 is inferred, as augmented for the various additional terms introduced through $\beta_i \neq 0$ in equation 39. The integration algorithm for equation 40 is the trapezoidal rule; hence,

$$\{FJ\} \equiv \{QJ\}_{j+1} - \{QJ\}_j - \frac{\Delta x_1}{2}[\{QJ\}'_{j+1} + \{QJ\}'_j] \equiv \{0\} \tag{41}$$

defines a system of nonlinear algebraic equations for determination of the elements of $\{QJ(x_1)\}$. A Newton iteration algorithm is employed for solution of equation 41 as

$$[J(FJ)]^p_{j+1}\{\delta QJ\}^{p+1}_{j+1} = -\{FJ\}^p_{j+1} \tag{42}$$

The dependent variable in equation 42 is the iteration vector, related to the solution $\{QJ\}_{j+1}$ in the conventional manner,

$$\{QJ\}^{p+1}_{j+1} = \{QJ\}^{p}_{j+1} + \{\delta QJ\}^{p+1}_{j+1} \tag{43}$$

The algorithmic embodiment of the differential constraint concept employs a sequential summation into the column matrix denoted $\vec{\beta}_2\int\nabla\{N_k\}L^p(\bar{\rho}^h)d\vec{x}$ in equation 39. A numerically determined optimum expansion coefficient is $\vec{\beta}_2 \equiv \Delta x_1\{\hat{j},\hat{k}\}$, where $\hat{j}$ and $\hat{k}$ are unit vectors parallel to x_ℓ. In the transverse plane momentum equations, this term corresponds to a load (column) matrix, say {G2PHI} for $\tilde{u}_2$. Letting $\{PHI\}^i_{j+1}$ denote the nodal solution for $\phi^h(x_\ell)$ at iteration step i then

$$\{G2PHI\}^i_{j+1} \equiv \hat{j}\cdot\nabla^h\{PHI\}^i_{j+1} \tag{44}$$

where ∇^h denotes the integral of the discrete gradient operator on the mesh of measure h. This contribution is then added to the sum of the previous p evaluations for ϕ^h, to construct the action of the differential constraint term for step $(\Delta x_1)_{j+1}$, iteration p+1, i.e.,

$$\{GU2\}^{p+1}_{j+1} \equiv \sum_{i=1}^{p} \{G2PHI\}^{i}_{j+1} \tag{45}$$

Hence, each successive determination of $\{PHI\}_{j+1}$ corrects the action of all previous solution iterates, such that $\{PHI\}^{p}_{j+1} \rightarrow \{\varepsilon\}$ as p increases without bound, where $|\varepsilon| > 0$ is an acceptable discrete level of computed zero. This procedure thus admits, in the limit, the exact continuity preserving solution for equation 30, i.e., $\phi \approx 0$ everywhere. Additional discussion on details of algorithmic constructions are given in the Appendix.

THEORETICAL ANALYSIS, ACCURACY AND CONVERGENCE

The 3DPNS equation system contains as a subset the two-dimensional boundary layer equations for laminar or turbulent flow. For these elementary systems, a finite difference truncation error analysis confirms the linear basis finite element formulation is spatially second-order accurate. Of course, the trapezoidal rule employed for chordwise marching is also second-order accurate. A formal analysis of convergence in Sobolev norms, [26] for a scalar linear parabolic equation, predicts the error ε^h in the semi-discrete linear basis finite element approximation q^h satisfies the inequality,

$$E\left(\varepsilon^h(n\Delta x_1),\varepsilon^h(n\Delta x_1)\right) \le C_1\Delta_e^2 \, ||q(n\Delta x_1)||_2^2 + C_2\Delta x_1^2 \, ||Q_0||_1^2 \qquad (46)$$

where C_1 is a constant independent of Δ_e, the measure of the largest finite element on R . Furthermore, C_2 is a constant independent of Δ_e, Δx_1 is the space-marching step, and $||Q_0||_1^2$ is the "energy" in the initial data. Hence, equation 46 confirms the solution error is bounded by a constant times a term of order Δ_e^2, i.e., second-order accurate. Furthermore, from the fundamental theorem [27], the semi-discrete approximate solution converges in energy, i.e.,

$$E(\varepsilon^h, \varepsilon^h) \rightarrow 0 \text{ as } \Delta_e \rightarrow 0 \qquad (47)$$

The strongly nonlinear 3DPNS (and turbulent boundary layer) differential equation systems are significant departures from the elementary equations considered in [26,27] . For example, the energy norm $E(\cdot,\cdot)$ is evaluated as

$$E\left\{q_j^h(n\Delta x_1),\ q_j^h(n\Delta x_1)\right\} = \sum_{e=1}^{M} \int_{R_e^n} \left[\bar{\nu}+C_4\ \frac{k^2}{\varepsilon}\right] \frac{\partial q_j^h}{\partial x_i}\ \frac{\partial q_k^h}{\partial x_i}\ \delta_{jk}\ d\vec{x} \tag{48}$$

The "effective" turbulent diffusion coefficient $\nu^t \equiv C_4 k^2/\varepsilon$ is a strongly non-linear function of q_j^h, with both k and ε exhibiting nearly singular behavior in the sub-layer region immediately adjacent to an aerodynamic surface. Nevertheless, the results of closely controlled numerical experiments [28, 29] have predicted extension of the linear theory, for the boundary layer equations, as well as providing exact comparisons between the $k = 1$ finite element algorithm, and the equal complexity (and familiar) Crank-Nicolson finite difference algorithm.

The fundamental theoretical aspect of critical importance is quantization of performance of the penalty continuity constraint on the transverse momentum equation solutions. The classical concept of the penalty construction for a linear elliptic statement [26] defines the parameter $\vec{\beta}_2 \Rightarrow \infty$ as the (norm of the) penalty term approaches zero. For the nonlinear parabolic Navier-Stokes system, and following extensive numerical experimentation, $\vec{\beta}_2 = \Delta x_1 [\hat{j}+\hat{k}]$ was determined preferable in optimizing the number of iterations/step to convergence. Using the outlined accumulation procedure, equations 44-45, the penalty algorithm yields satisfaction of the continuity equation in energy to the order of $E(\phi^h, \phi^h \approx O(10^{-8})$ for laminar boundary layer flow, $E(\phi^h, \phi^h) \approx O(10^{-6})$ for turbulent boundary layer flow, and $E(\phi^h, \phi^h) \approx O(10^{-5})$ for 3DPNS solutions.

PROBLEM ANALYSES

Idealized Wing-Body Juncture Flow

The documentary test case configuration, for the developed 3DPNS algorithm and the CMC:3DPNS computer program, is turbulent flow in the juncture region formed by the right intersection of two 10-percent thick parabolic arcs with coincident leading edge. A complete discussion of the CMC:3DPNS program input and data deck preparation procedures is presented in Volume II of this report. The computer program documentation manual for the CMC:3DPNS code is published as Volume III.

Figure 2a illustrates the essential geometry of the parabolic arc juncture specification. The complementary pressure (p_c) boundary conditions for the 3DPNS solution were obtained using the Hess potential flow computer code [30], for $M_\infty = 0.08$ ($U_\infty = 30$ m/s ≈ 100 f/s) and zero angle of attack. Figure 2b) summarizes the resultant spanwise distributions of $p_c(\bar{x}_\ell)$ at chord stations $x_1/C = 0.01$, 0.085, and 0.46. By symmetry, these pressure boundary conditions are also appropriate at $x_1/C = 0.54$, 0.915, and 0.99. Therefore, a progressively decreasing favorable x_1 pressure gradient exists to mid-chord, and thereafter turns progressively adverse. The strongest gradients are confined to the immediate vicinity of the corner.

The 3DPNS solution domain was defined to span $0 \leq x_\ell/C \leq 0.1$ and of height $x_k/C \approx 0.01$. Figure 3 illustrates a nonuniform discretization of the transverse plane R^2 as the union of triangles (with most diagonals omitted for clarity). The domain boundary ∂R is the union of straight line segments A-F, upon which boundary condition specifications are required for the dependent variable set $q_i^h(x_\ell, x_1)$, see Table 1. The Reynolds number is $Re/C = 0.6 \times 10^6$/m, and the flow is assumed isoenergetic, hence $\tilde{H}(x_i) =$ constant. The initial conditions for $u_1^0(x_\ell)$, at the nodes of R^2, are established using Cole's law to interpolate a turbulent boundary layer profile onto node "columns," Figure 3, with matching of the free-stream level of $p_c(\bar{x}_\ell)$. The transverse plane velocity $\tilde{u}_\ell(x_\ell)$ is defined identically zero, until eight 3DPNS steps are completed, to permit computation of a reasonable chordwise derivative of $\bar{\rho}\tilde{u}_1$, e.g., $\{RHOU1\}'$. The initial distributions for $k^0(x_\ell)$ and $\varepsilon^0(x_\ell)$ are computed using boundary layer mixing length concepts, as discussed in detail in [23]. Each

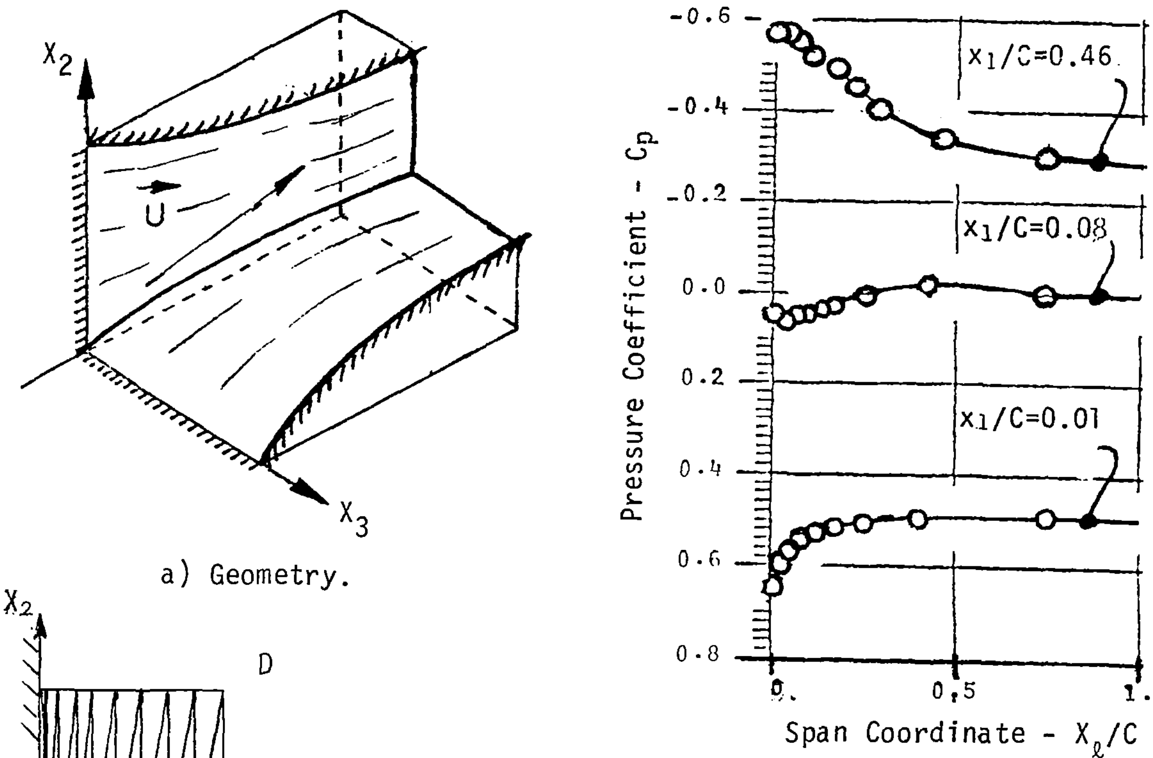

a) Geometry.

b) Inviscid Pressure Distribution

Figure 2. Characterization of 10-Percent Thick Parabolic Arc Juncture Region.

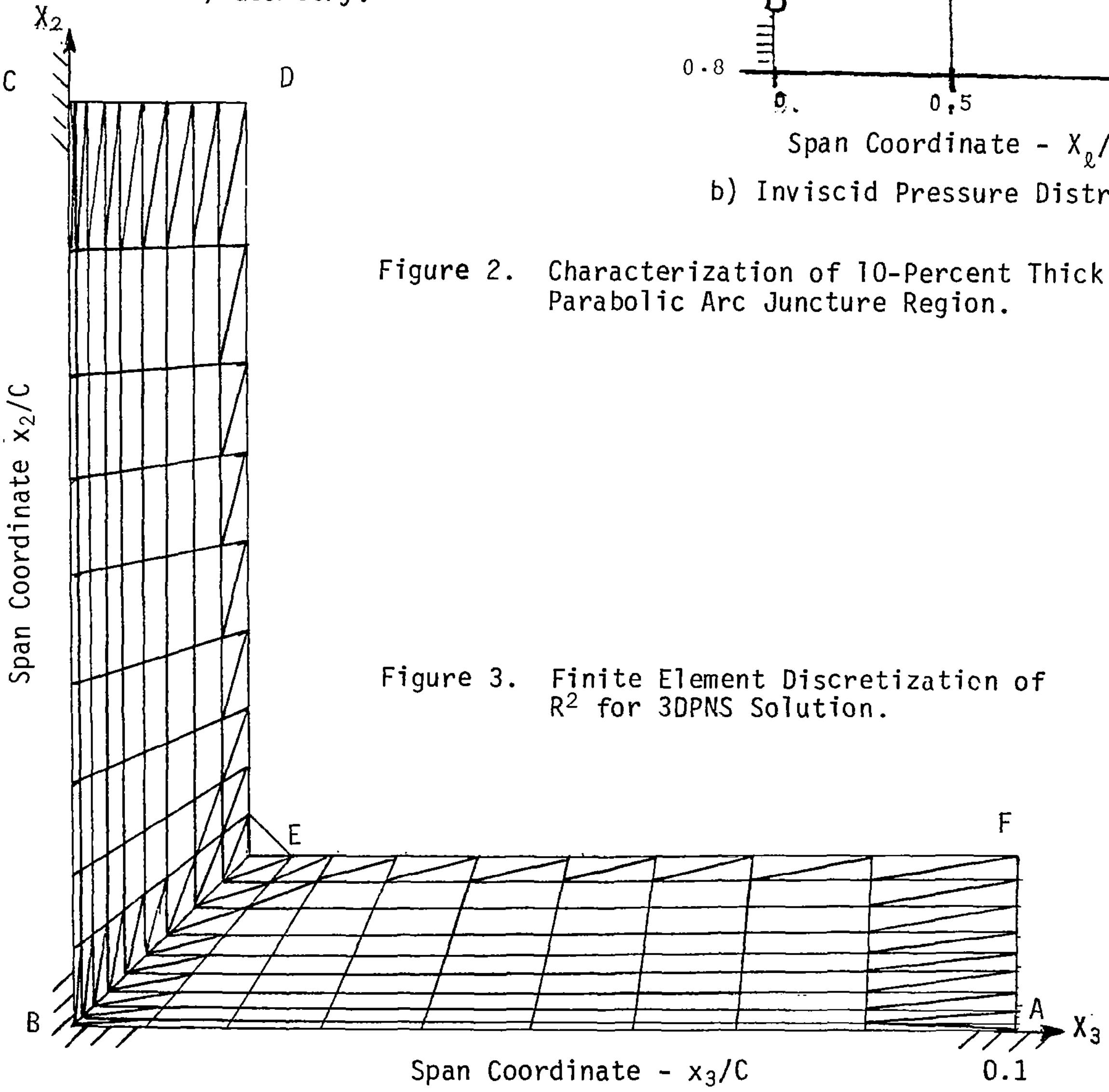

Figure 3. Finite Element Discretization of R^2 for 3DPNS Solution.

TABLE 1

Boundary Condition Specifications for 3DPNS Analysis of Aerodynamic Juncture Region Flow

Dependent Variable	Equation No.	Boundary Segment	Boundary Condition Statement, Equation 35			Comments
			a_1	a_2	a_3	
$\tilde{u}_1$	11	ABC	1	0	0	No-slip Surface
		CDEFA	0	1	0	Vanishing Derivative
$\tilde{u}_\ell$	29	ABC	1	0	0	
		CDEFA	0	1	0	
k	23	ABC	1	0	0	
		CDEFA	0	1	0	
ε	24	ABC	1	0	0	
		CDEFA	0	1	0	
p_c	16	DEF	1	0	$\bar{p}$	Potential Constraint
		FABCD	0	1	0	
p_p	14	ABC	1	0	0	
		CDEFA	0	1	0	
ϕ	30	DEF	1	0	0	
		FABCD	0	1	0	

of these initialization procedures is a CMC:3DPNS input specification, discussed in detail in Volume II.

The standard test case specification is 3DPNS solution of the parabolic arc juncture region turbulent flow on the interval $0.01 \le x_1/C \le 0.60$, using the 10 X 19 node nonuniform discretization shown in Figure 3. The corresponding number of triangular finite element domains is $M = (10-1)X(19-1)X2 + 1 = 325$. On this grid, the 3DPNS algorithm takes 170 chordwise steps and averages 4.3 Newton iterations/step for convergence set at $\varepsilon = 0.0003$. On the NASA Langley CDC Cyber/203 computer, with no vectorization of the scalar CMC:3DPNS code, this execution requires 475 seconds of CPU time. For comparison, the same execution on an IBM 370/3031 computer requires approximately 6000 seconds of CPU time. The central memory requirement for both executions is 150,000 words. During the 3DPNS solution, the distribution of the particular pressure solution $p_p(x_\ell,x_1)$ is written on an output file at each chordwise station x_1 for which the $p_c(\bar{x}_\ell, x_1)$ boundary condition is specified. For the second and sequential 3DPNS solutions, the solution of equation 16 for $p_c(x_\ell,x_1)$ is algebraically summed with the stored distributions $p_p(x_\ell, x_1)$, see equation 15, and this sum employed for the chordwise pressure gradient distribution for the $\tilde{u}_1$ momentum equation solution, see equation 11. The $\tilde{u}_\ell$ momentum equations are solved using the current computed p_p distributions. The composite pressure field $p(x_i)/p_0$, equation 15, converges to five significant digits following three 3DPNS algorithm solutions, for the standard test juncture region geometry. The nominal level of p_p/p_0 is 10^{-3}; a representative extremum difference between the second and third 3DPNS solutions is $\Delta p_p/p_0 \approx 10^{-5}$ at $x_1/C = 0.17$.

The 3DPNS solution computes and outputs the distribution of $q_j^h(x_\ell,x_1)$ at select chordwise stations x_1. Figures 4-5 illustrate qualitatively the third interaction 3DPNS solution for transverse velocity $\tilde{u}_\ell$ for the parabolic arc juncture. Figure 4 graphs the complete transverse plane velocity distribution $\tilde{u}_\ell(x_\ell)$ at $x_1/C = 0.31$ on the $M = 325$ grid. The solution is exactly mirror symmetric, a generated vortex pair in the corner is just distinguishable, and the solution computes a spanwise efflux of $\tilde{u}_\ell$ from the 3DPNS domain. Figure 5 summarizes the $M = 325$ grid solution evolution of the lower surface distribution of $\tilde{u}_\ell(x_\ell)$ on $0.021 \le x /C \le 0.7$. (The truncated upper portions

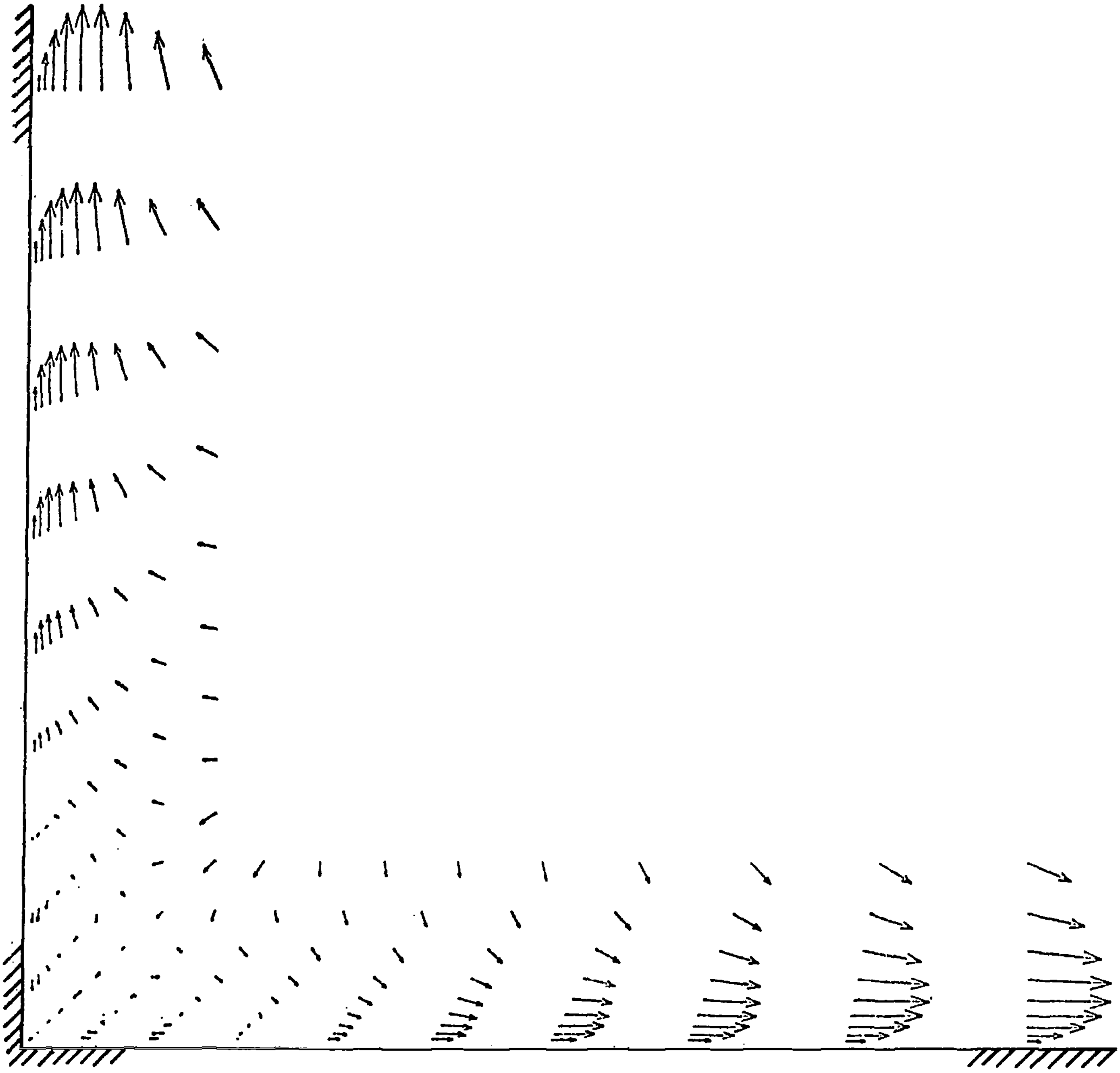

Figure 4. 3DPNS Solution for Transverse Plane Velocity $\tilde{u}_\ell$ Distribution, Parabolic Arc Juncture Region, $x_1/C = 0.40$, $M = 325$, Turbulent Flow.

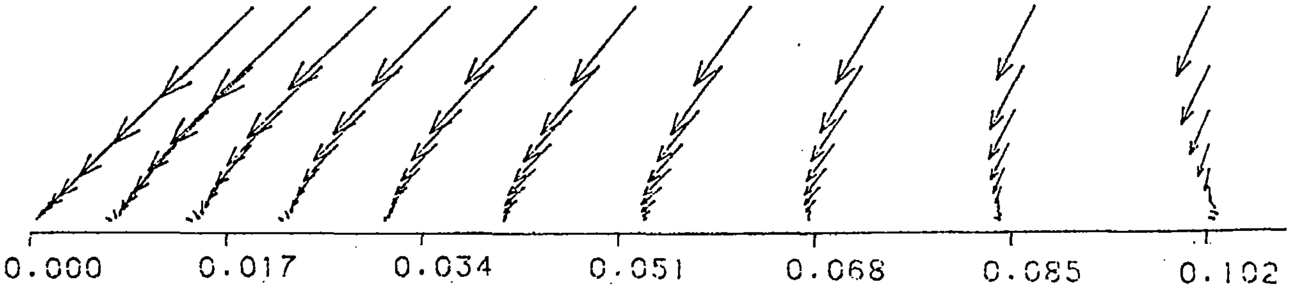

a) $x_1/C = 0.021$, $\tilde{u}^m_\ell/\tilde{u}_1 = 0.167$

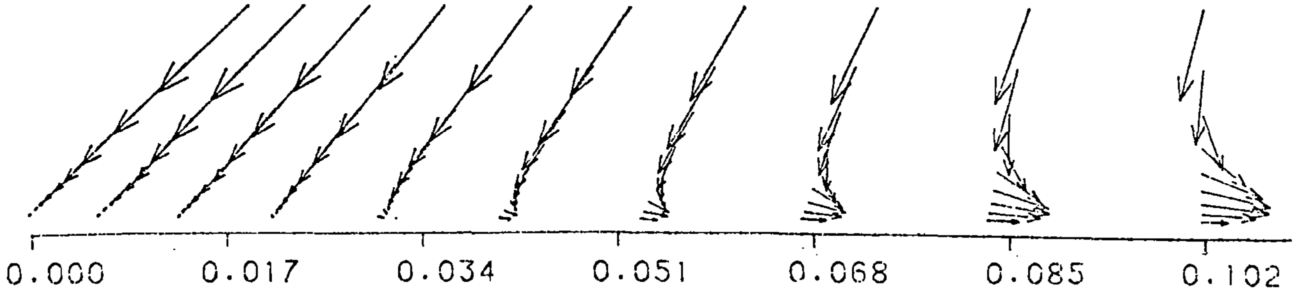

b) $x_1/C = 0.047$, $\tilde{u}^m_\ell/\tilde{u}_1 = 0.072$

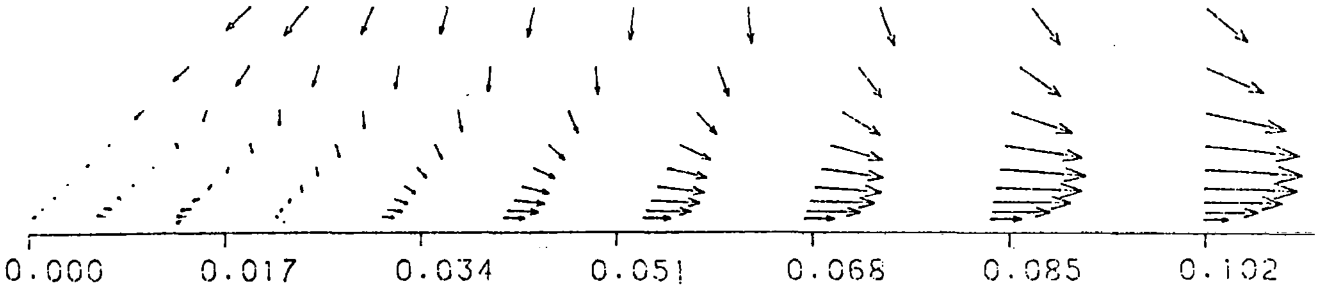

c) $x_1/C = 0.081$, $\tilde{u}^m_\ell/\tilde{u}_1 = 0.058$

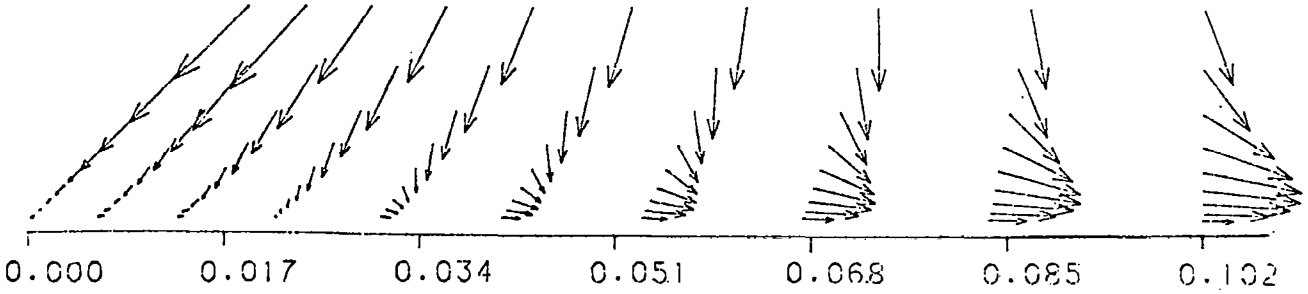

d) $x_1/C = 0.173$, $\tilde{u}^m_\ell/\tilde{u}_1 = 0.112$

Figure 5. 3DPNS Solution for Transverse Plane Velocity $\tilde{u}_\ell$ Distributions, Parabolic Arc Juncture Region, Turbulent Flow.

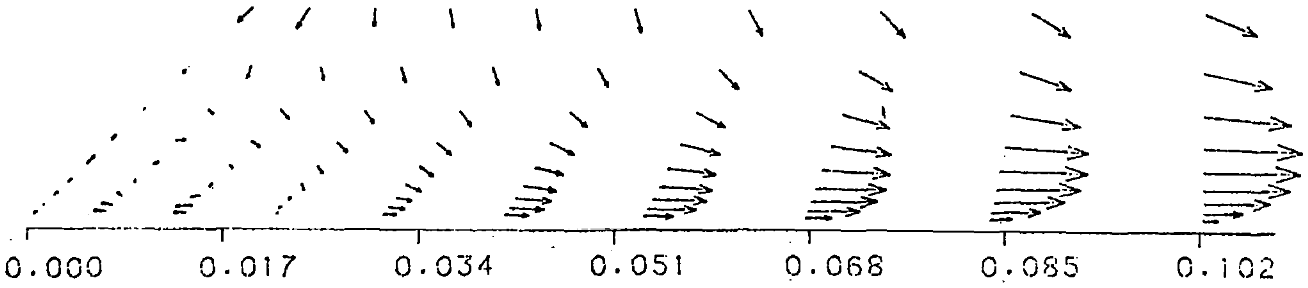

e) $x_1/C = 0.349$, $\tilde{u}^m/\tilde{u}_1 = 0.114$

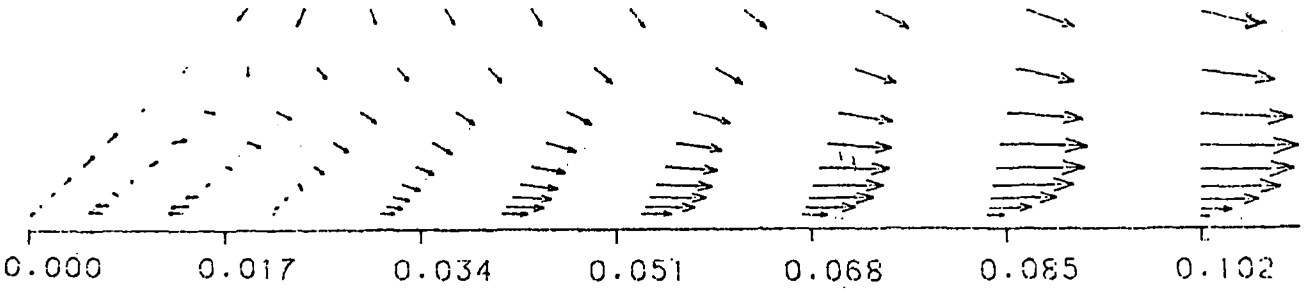

f) $x_1/C = 0.502$, $\tilde{u}^m_\ell/\tilde{u}_1 = 0.102$

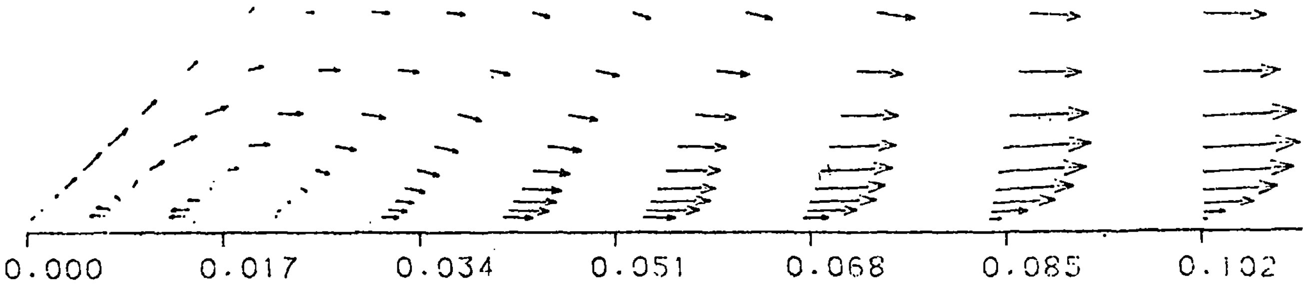

g) $x_1/C = 0.631$, $\tilde{u}^m_\ell/\tilde{u}_1 = 0.098$

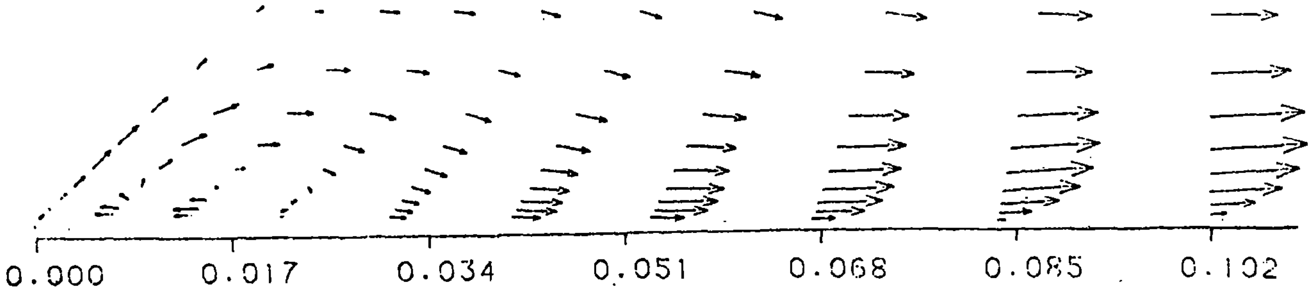

h) $x_1/C = 0.704$, $\tilde{u}^m_\ell/\tilde{u}_1 = 0.097$

Figure 5. Concluded.

are exactly mirror symmetric.) A massive influx into the corner region is predicted at $x_1/C = 0.021$, with the extremum scalar component $\tilde{u}_\ell^m/\tilde{u} = 0.167$, i.e., equal to 17% of the local free-stream value of $\tilde{u}_1$. This is the direct result of the associated large favorable pressure gradient for $\tilde{u}_1$, coupled with the fact that the mass conservation algorithm has just become initialized. By $x_1/C = 0.047$, the extremum scalar component is $\tilde{u}_\ell^m/\tilde{u}_1 = 0.072$, and the juncture blockage is inducing a large spanwise efflux from R^2 in the lower reaches of the boundary layer. A corner axial vortex (pair) is just visible at $x_1/C = 0.081$, where the minimum level of $\tilde{u}_\ell$ is predicted. This general velocity distribution persists to well beyond mid-chord, with $\tilde{u}_\ell^m/\tilde{u}_1 \approx 10\%$ throughout. The corner vortex pair becomes fully developed, with the spanwise efflux filling the entire boundary layer. Past mid-chord, the free-stream velocity derivative changes sign, with a concurrent cessation of influx from the potential region into the corner indicated by $x_1/C = 0.63$.

A repeating of this solution for laminar flow provides an additional qualitative accuracy assessment. Figure 6 compares the 3DPNS transverse plane velocity distributions at $x_1/C = 0.46$, for laminar and turbulent flow solutions. In comparison, the corner vortex pair is slightly larger for laminar flow, the extremum component $\tilde{u}_\ell^m/\tilde{u}_1 = 0.06$ is 40% smaller in magnitude, and a reversed spanwise flow is predicted in the lowest reach of the farfield boundary layer, Figure 6a). Shafir and Rubin [31] predict theoretically this lower reach reversal, for laminar-turbulent boundary layer transition, see Figure 7. Furthermore, the flow-fields in Figure 6 are in qualitative agreement with the composite corner layer/asymptotic boundary layer solution reported by Rubin and Grossman [3].

Figure 8 is a composite summary of pertinent transverse plane isoclines of $\tilde{u}_1$ and components of $\overline{u_i' u_j'}$ at $x_1/C = 0.46$, as predicted by the third interaction 3DPNS solution. The $\tilde{u}_1$ solution exhibits the intrinsic symmetry with a modest relative displacement directly adjacent to the corner, the result of the axial vortex pumping low momentum fluid into the corner and out parallel to the diagonal, Figure 6(b). The plot of $\overline{u_1' u_1'}$ is also symmetric, and a local extrema exists in the corner due to the axial vortex pumping of the wall layer

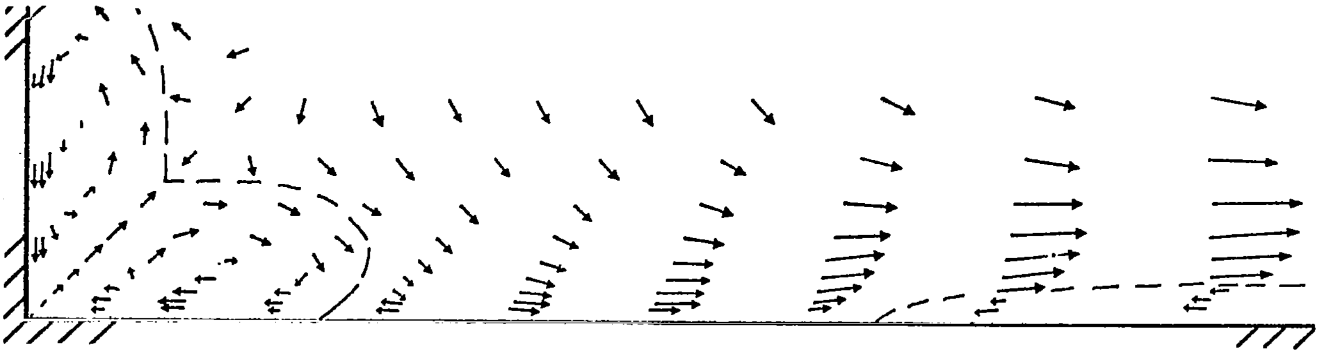

a) Laminar Flow, $\tilde{u}_{\ell}^{m}/\tilde{u}_1 = 0.06$.

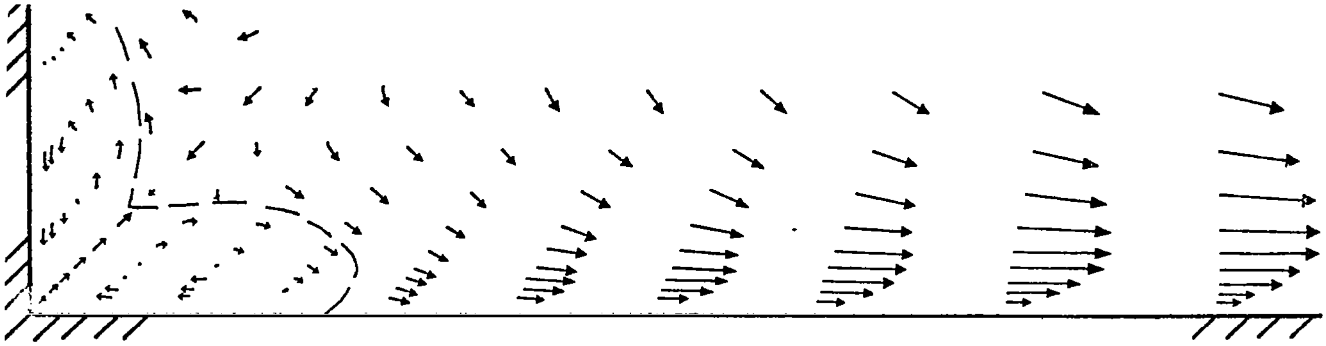

b) Turbulent Flow, $\tilde{u}_{\ell}^{m}/\tilde{u}_1 = 0.10$.

Figure 6. 3DPNS Solution Transverse Plane Velocity $\tilde{u}_{\ell}$ Distribution, Juncture Region Flow, $x_1/C = 0.46$.

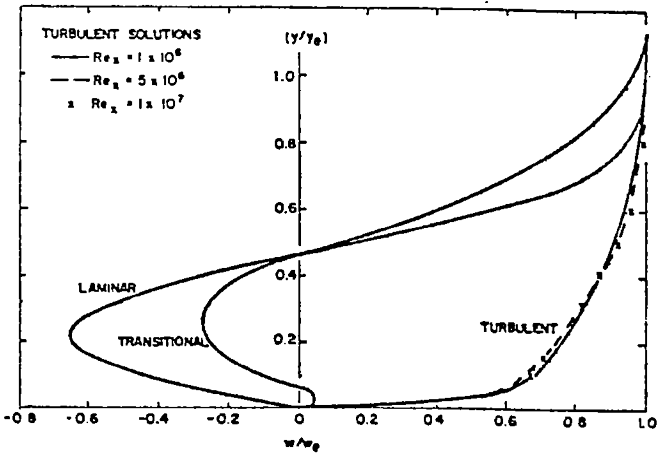

Figure 7. Boundary Layer Laminar/Turbulent Transition Solutions In Juncture Region Farfield, from Shafir and Rubin [31]

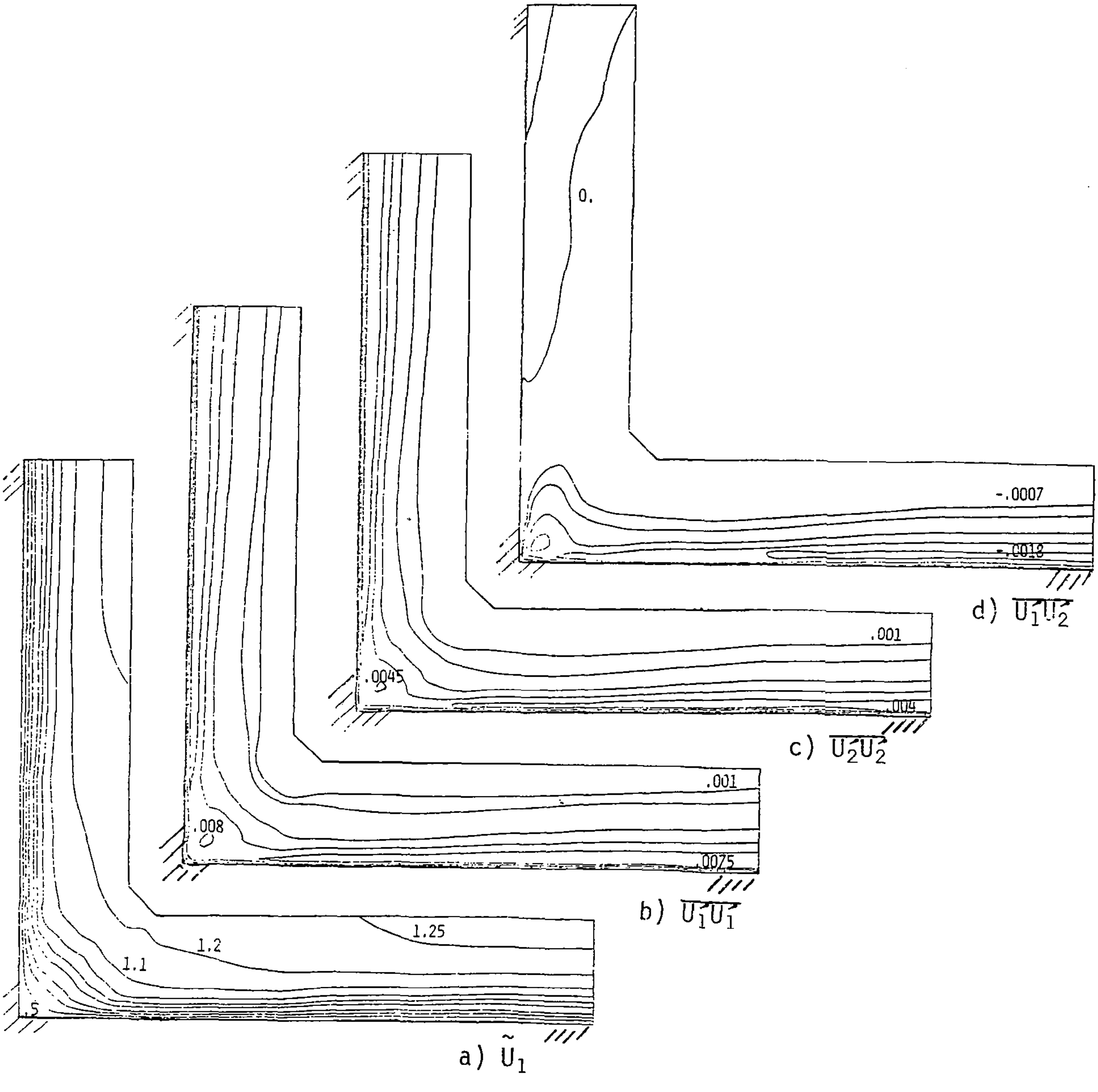

Figure 8. 3DPNS Solution Summary, Parabolic Arc Juncture Region, Turbulent, $Re/C = 6.X\ 10^5$, $M_\infty = 0.08$, $x_1/C = 0.46$.

flow into the corner. These comments are valid for the distribution of $\overline{u_2'u_2'}$, except that this normal stress exhibits a (very) modest nonsymmetry due to the $O(\delta)$ terms involving $\tilde{u}_1$ in equation 22. The $\overline{u_1'u_2'}$ shear stress distribution is highly nonsymmetric with the extremum level penetrating only half the span distance to the corner. On the upper-half domain, these levels are very small since $\tilde{u}_1(x_2)$ is a weak function of x_2 along the vertical span. Of course, $\overline{u_1'u_3'}$ is a mirror symmetric reflection of $\overline{u_1'u_2'}$.

Reynolds Stress Closure Verification

No complete experimental data set exists for quantitative comparison of the juncture region turbulent flow 3DPNS prediction. For this geometry, the initially steep chordwise pressure gradient is principally responsible for generation of the axial vortex pair. Thereafter, in the mid-chord region, the combined action of milder pressure gradients and Reynolds stress distributions govern the detailed flow-field evolution. The typical experimental juncture region geometry, cf. [12, 13], is constructed as the right intersection of two plane surfaces with noncoincident leading edge. One surface is the wind tunnel floor, while the second is a rounded leading edge, nonfilletted, finite thickness flat plate mounted perpendicular to the floor. The resultant three-dimensional, separated stagnation region flow yields a pressure-gradient induced roll vortex, in the "wing" leading edge region, which is then convected downstream under nominal zero axial pressure gradient.

An experimental configuration that specifically facilitates the Reynolds stress closure verification is turbulent flow in a straight, uniform rectangular cross-section duct, cf. [11]. Following the localized entrance region effects, the mild axial pressure gradient is nominally uniform on the cross-section and of magnitude sufficient to compensate for duct friction losses. Far downstream, experiments verify that no consequential transverse plane velocities exist for laminar flow. Conversely, for a turbulent flow, four persistent axial vortex pairs exist, one in each right angle corner of the duct. For the experimental specification of [11], Baker and Orzechowski [32] document qualitative agreement for the 3DPNS algorithm prediction on a coarse 13X13 (M = 288) discretization of the symmetric quarter duct. Specifically, no vortex pair roll-up occurred for the laminar flow, or for the turbulent flow prediction with the $O(\delta)$ terms involving $\tilde{u}_1$ derivatives in $\overline{u_\ell'u_\ell'}$ set to zero, see equation 22.

However, with these terms included, as required theoretically by invariance within the constitutive theory, the turbulent flow 3DPNS prediction immediately generated the corner vortex pair. Therefore, in this instance of a nonpressure driven flow, the anisotropy of the Reynolds stress tensor is principally responsible for generation of the axial vortex pair.

With the CMC:3DPNS code now operational on the CDC Cyber/203, refined grid and full-duct solutions for the configuration of [11] have been executed for quantitative comparison to experimental data [11] for transverse plane distributions of $\tilde{u}_i$ and $\overline{u_i' u_j'}$ at a downstream station. Figure 9a), from [11], is the experimental measurement, of transverse plane velocity distribution $\tilde{u}_\ell(x_1 = 37, x_\ell)$, with $\tilde{u}_\ell^m/\tilde{u}_1 = 0.0086$. Figure 9b), from [32], is the coarse (M = 288) grid 3DPNS solution on the symmetric quarter duct, which exhibits essential qualitative agreement with data. However, $\tilde{u}_\ell^m/\tilde{u}_1 = 0.0010$ is a factor of eight lower than the data, and large vortex patterns are erroneously produced adjacent to both symmetry planes. Figure 9c) is the refined (M = 1052) grid solution on the symmetric quarter duct. The qualitatively correct vortex patterns nearly fill the section, and $\tilde{u}_\ell^m/\tilde{u}_1 = 0.0043$ is only a factor of two lower than the data. The erroneous vortices remain predicted next to both symmetry planes, but their size is substantially reduced in comparison to Figure 9b). The combined M = 288 and M = 1052 solutions confirm that the error mechanism causing this local pollution of the solution is a singularity in the boundary conditions for the mass conservation harmonic function $\phi^h(x_\ell)$, where the symmetry plane intersects the wall. Since a velocity component is permitted (must occur) parallel to the symmetry plane, but not along the no-slip wall, the intersection corresponds to a discontinuous switch from homogeneous Dirichlet to homogeneous Neumann boundary conditions at a corner. Removal of this singularity requires the 3DPNS solution domain to span the full duct cross-section. The 3DPNS solution executed on a coarse (M = 1052) grid discretization of the entire duct, did predict extinction of the spurious vortices. However, the extremum transverse velocity $\tilde{u}_\ell^m/\tilde{u}_1 = 0.0020$ is a factor of four lower than data, indicating the discretization too coarse for qualitative solution comparison. Hence, a 50 X 50 ($M \approx 2500$) discretization is thus indicated as the refinement required for a 3DPNS simulation of a ducted turbulent flow.

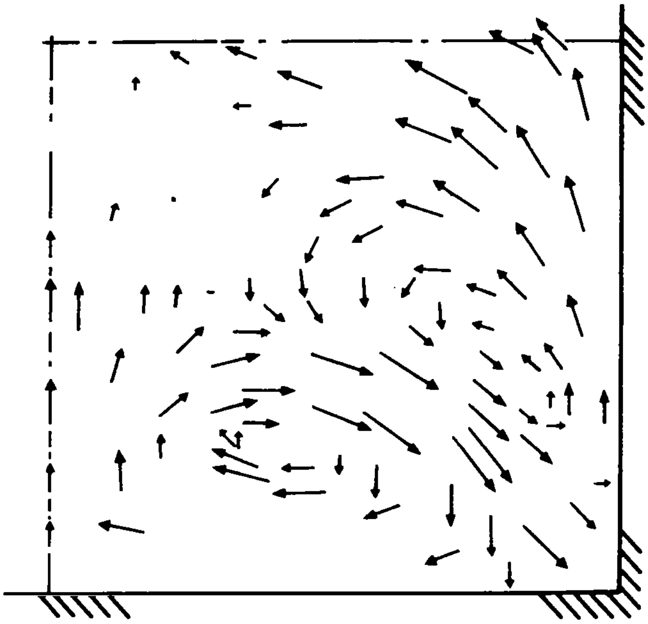

a) Experimental [11]

$\tilde{u}^m_\ell/\tilde{u}_1 = 0.0086.$

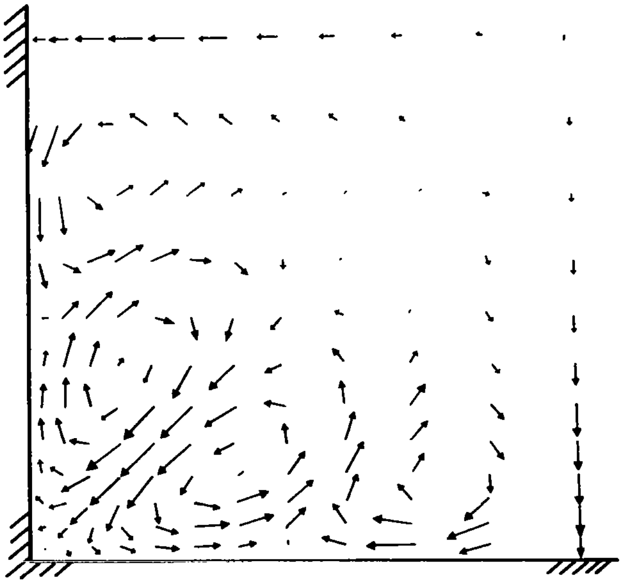

b) 3DPNS Solution [32]

M = 288

$\tilde{u}^m_\ell/\tilde{u}_1 = 0.0010.$

Figure 9. 3DPNS and Experimental Distributions of Transverse Plane Velocity $\tilde{u}_\ell$, Turbulent Rectangular Duct Flow.

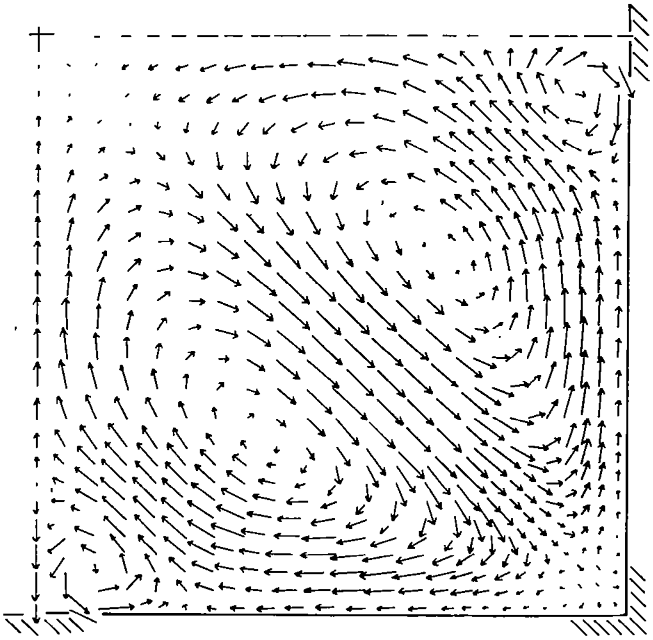

c) 3DPNS Solution, M = 1052, $\tilde{u}^m_\ell/\tilde{u}_1$= 0.0043

Figure 9. Concluded

Reference [11] also documents experimentally measured distributions of $\tilde{u}_1$, k, and $\overline{u_i' u_j'}$ at the downstream station. Figures 10-17 compare these data with the 3DPNS solution obtained on the M = 1052 quarter-duct discretization. Figure 10a) indicates intrusion of the high momentum core velocity $\tilde{u}_1$ into the corner region, as induced by the vortex structure, Figure 9a). The 3DPNS solution exhibits this character for $\tilde{u}_1 \leq 0.70$ only, Figure 10b). The intersection of the 3DPNS $\tilde{u}_1 = 0.70$ isovel with the symmetry plane is in good agreement with experiment. Above this level, and on the symmetry planes, the intersection of 3DPNS levels for $\tilde{u}_1$ exceed data by $\Delta x_\ell \approx 15\%$. Along the corner bisector, the levels are in better agreement.

Figures 11-13 compare the Reynolds shear stress distributions. Good overall agreement on level is indicated, as well as some detail of the contour shapes for the largest levels. The experimentally measured regions of small negative ($\overline{u_1' u_2'}$) and small positive ($\overline{u_1' u_3'}$) shear stress result from the curve inflections in $\tilde{u}_1$, Figure 10a). The 3DPNS solution has correctly predicted this essential character, although the details are largely affected by the boundary condition singularity effects. This is clearly illustrated by the "ears" on the 3DPNS prediction of $\overline{u_2' u_3'}$, Figure 13. No experimental determination of this shear stress component is reported in [11], since the signal to noise ratio at $O(10^{-4})$ is essentially unresolvable.

Figures 14-17 summarize the comparison of the square root of the Reynolds normal stresses and the turbulence kinetic energy level. Overall, the agreement on levels of $\overline{u_i'}$ is good, confirming use of the standard definitions for the constitutive equation model constants C_α, equation 22, and the coefficients C_α^β in equations 23-24. The 3DPNS prediction for $\overline{u_1'}$ and k, Figures 14-15, are symmetric in agreement with data. The intrusion of the lower levels from the core region along the bisector is substantially under-predicted. The intersection of $\overline{u_1'} = 0.075$ on the symmetry plane is in good agreement, and the higher 3DPNS solution levels exhibit better agreement with data. The intersection of $\overline{u_1'} = 0.05$ is different by $\Delta x_\ell \approx 20\%$, indicating the level of turbulence in the experimental core flow is considerably larger than that of the 3DPNS simulation, see also Figure 15. The 3DPNS solution initialization level of $k^0 \approx 10^{-6}$ in the potential core region is considerably smaller (probably) than the experiment.

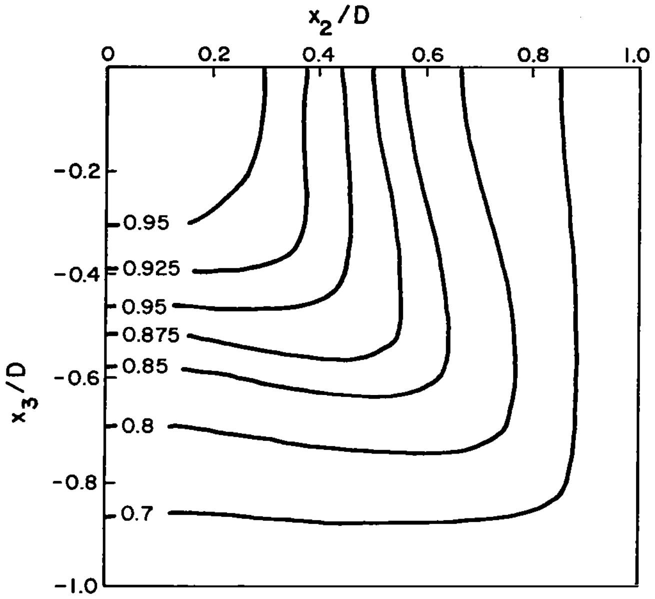

a) Experimental [11]

$x_1/D = 37.0.$

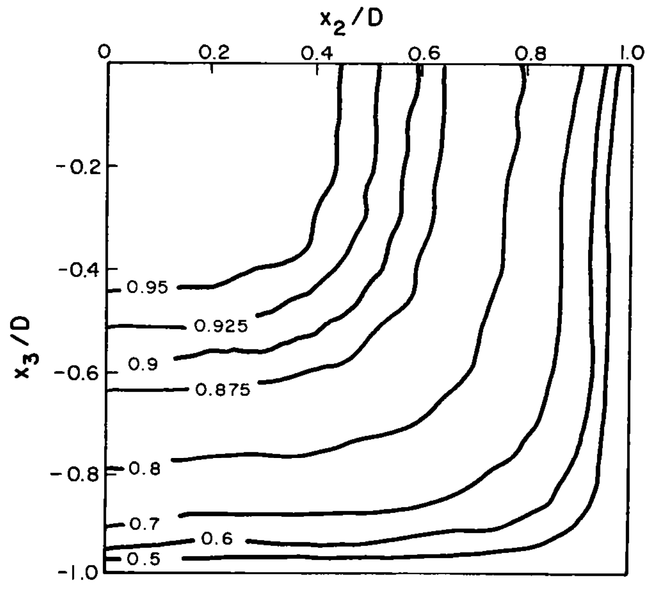

b) 3DPNS Solution

$x_1/D = 35.8.$

Figure 10. 3DPNS and Experimental Distributions, Mean Velocity $\tilde{u}_1$, Turbulent Rectangular Duct Flow.

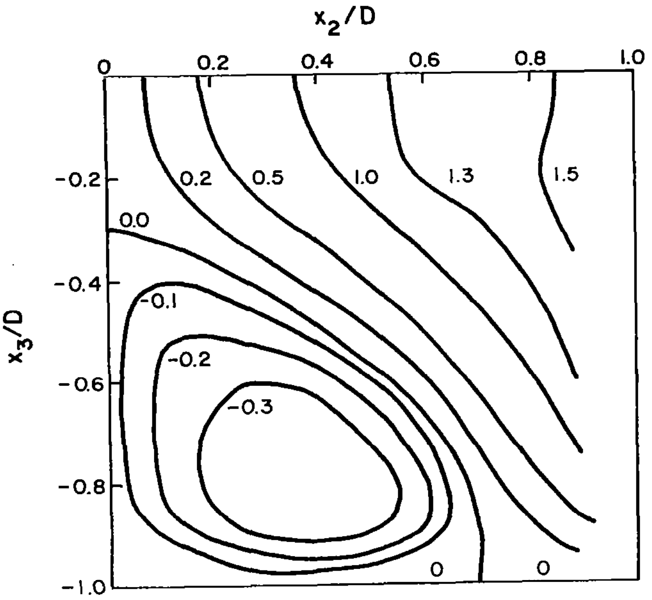

a) Experimental [11]
$x_1/D = 37.0$.

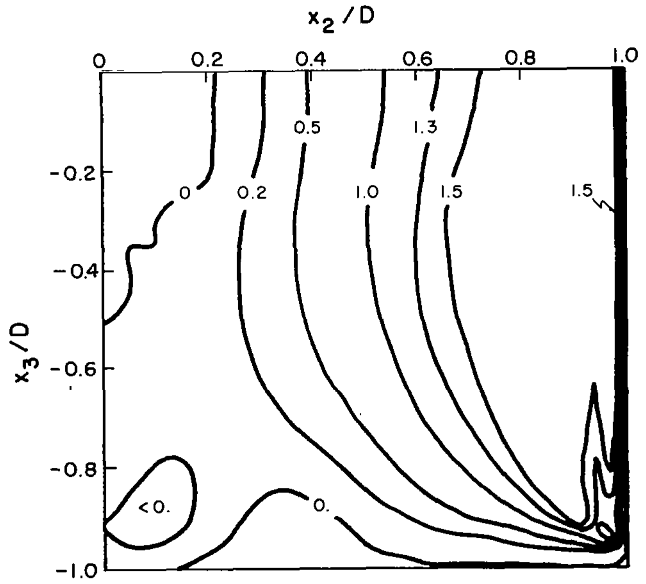

b) 3DPNS Solution
$x_1/D = 35.8$.

Figure 11. 3DPNS and Experimental Distributions, Reynolds Shear Stress $-\overline{u_1 u_2}$ X 10^3 , Turbulent Rectangular Duct Flow.

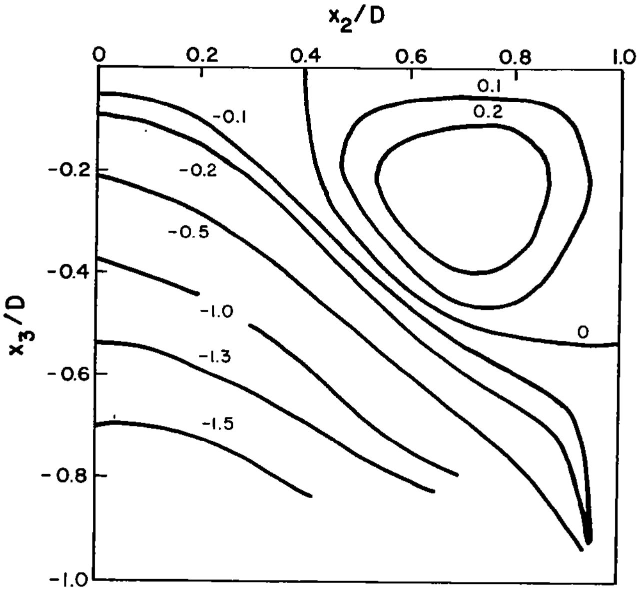

a) Experimental [11]
x_1/D = 37.0

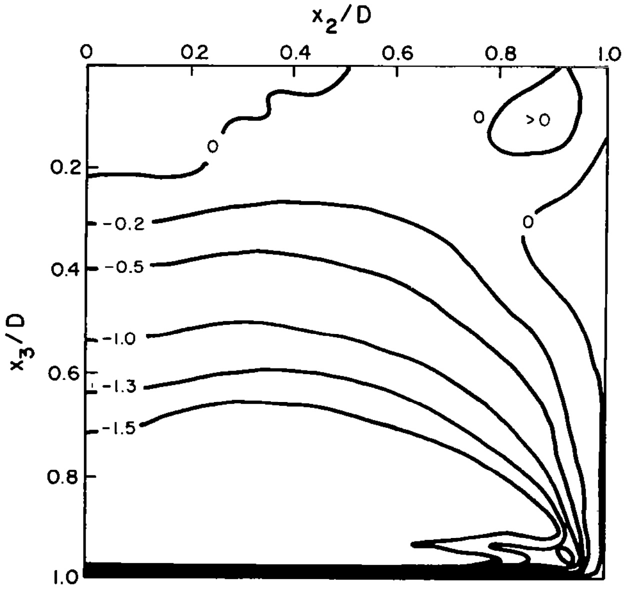

b) 3DPNS Solution
x_1/D = 35.8

Figure 12. 3DPNS and Experimental Distributions, Reynolds Shear Stress $-\overline{u_1'u_3'}$, X 10^3, Turbulent Rectangular Duct Flow.

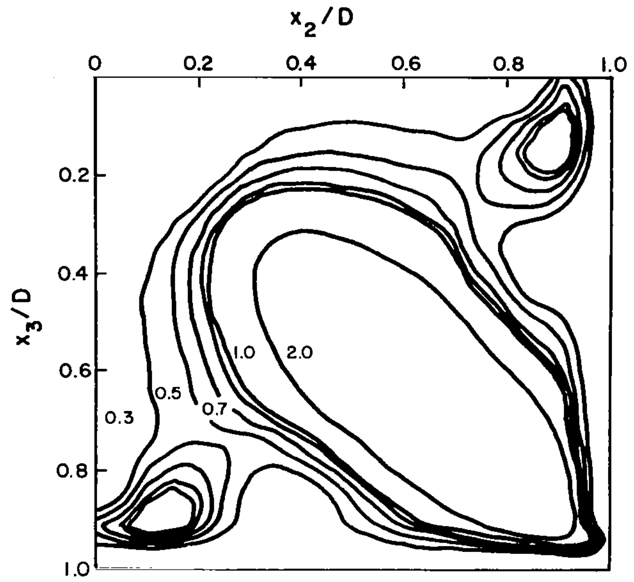

Figure 13. 3DPNS Solution Distribution - Reynolds Shear Stress $-\overline{u_2'u_3'}$X 10^4, Turbulent Rectangular Duct Flow.

Figures 16-17 compare the transverse plane normal stress distributions. Agreement on overall levels is considerably better, with the 3DPNS prediction exhibiting the essential nonsymmetries of the experimental data. Note the two 3DPNS solutions are mirror symmetric, while the data are less so. Most importantly, recall that these (modest) nonsymmetries are computationally confirmed to be the principal causal mechanism of the counter-rotating vortex structure for turbulent flow in a straight, rectangular cross-section duct.

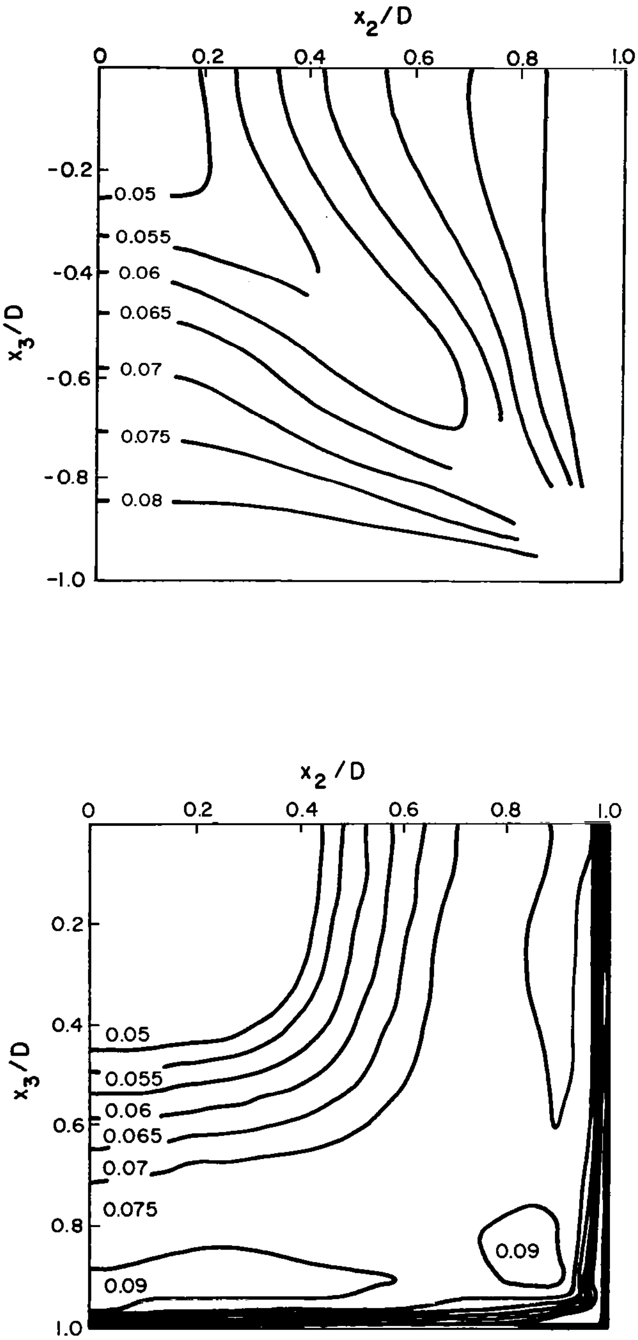

a) Experimental [11]

$x_1/D = 37.0$.

b) 3DPNS Solution

$x_1/D = 35.8$.

Figure 14. 3DPNS and Experimental Distributions, Reynolds Normal Stress $-\sqrt{\overline{u_1' u_1'}}$, Turbulent Rectangular Duct Flow.

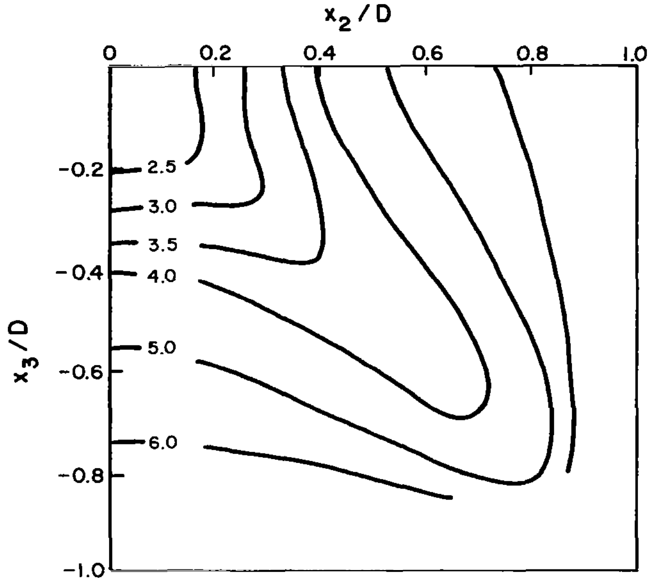

a) Experimental [11]

$x_1/D = 37.0$.

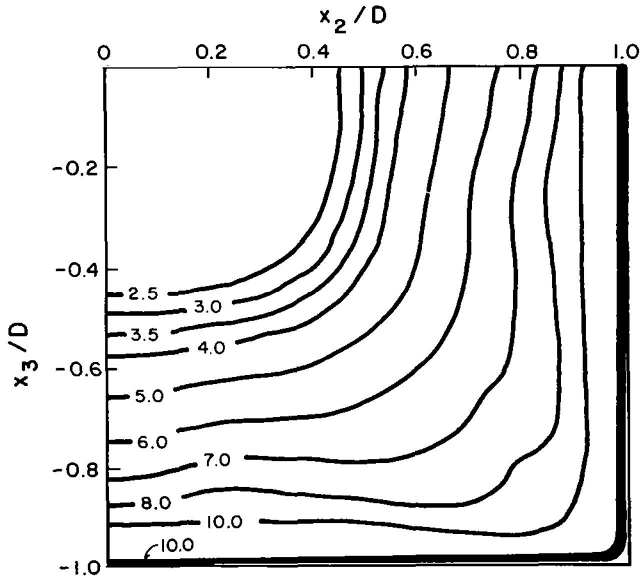

b) 3DPNS Solution

$x_1/D = 35.8$.

Figure 15. 3DPNS and Experimental Distributions of Turbulent Kinetic Energy $k \times 10^3$, Turbulent Rectangular Duct Flow.

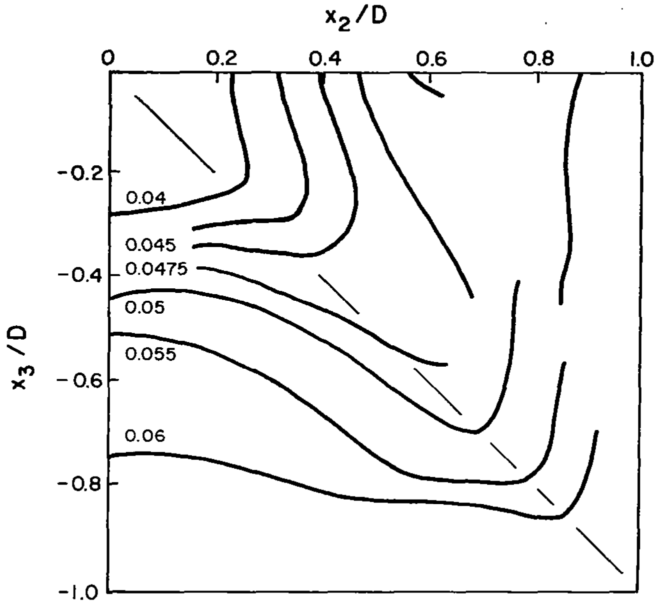

a) Experimental [11]

$x_1/D = 37.0$.

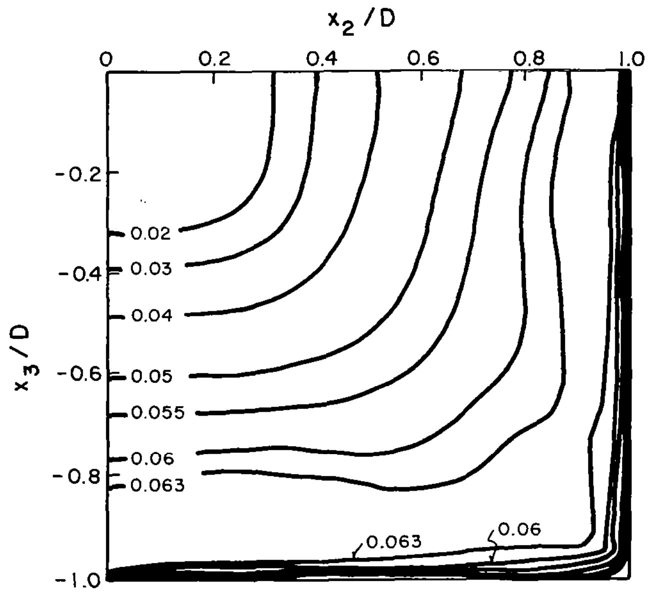

b) 3DPNS Solution

$x_1/D = 35.8$.

Figure 16. 3DPNS and Experimental Distributions, Reynolds Normal Stress $-\sqrt{\overline{u_2'u_2'}}$, Turbulent Rectangular Duct Flow.

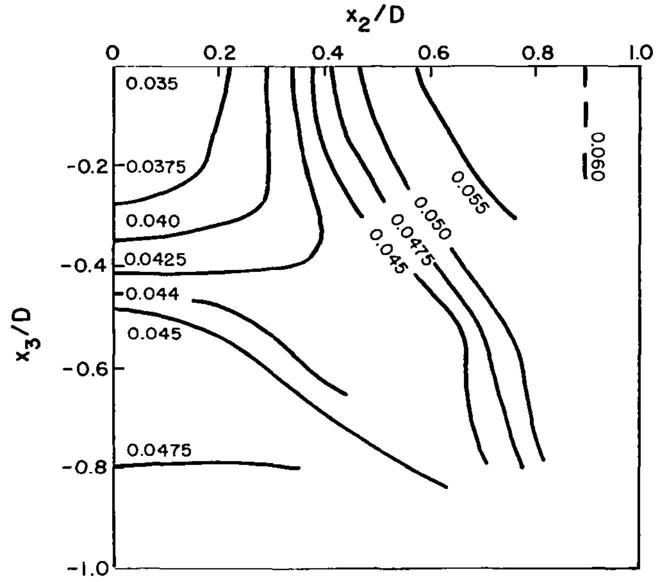

a) Experimental [11]

$x_1/D = 37.0$.

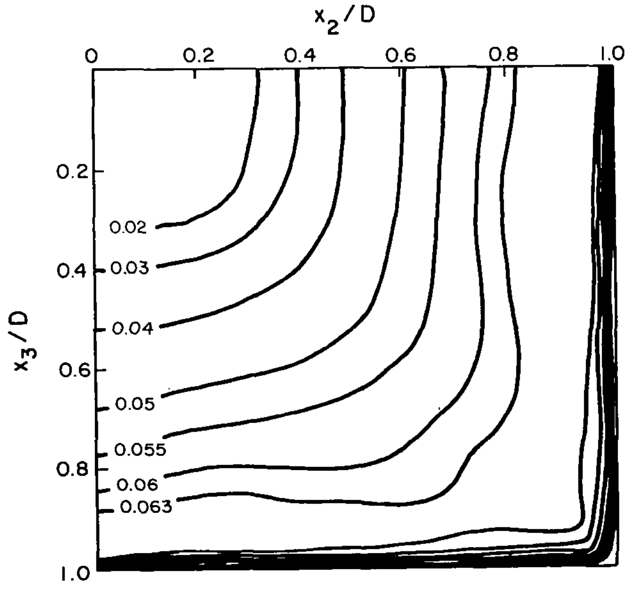

b) 3DPNS Solution

$x_1/D = 35.8$.

Figure 17. 3DPNS and Experimental Distributions, Reynolds Normal Stress $-\sqrt{\overline{u_3' u_3'}}$, Turbulent Rectangular Duct Flow.

CONCLUSIONS

An order of magnitude analysis has yielded a consistent physical variables formulation for the parabolic approximation to the three-dimensional Navier-Stokes equations for steady, turbulent subsonic flow. A finite element numerical solution algorithm is derived that accurately enforces the dominant differential equation set through formulation of a penalty differential constraint statement. A tensor field expansion is employed to provide closure for the Reynolds stress distribution, in concert with solution of two turbulent transport equations. A composite pressure field construction is identified to enforce overall ellipticity, using a multipass interaction solution procedure with a three-dimensional potential flow exterior solution. Numerical results document the robustness of the key elements of the developed algorithm for the aerodynamic juncture region geometry.

APPENDIX

The finite element algorithm statement for the 3DPNS equation system is readily recast into equivalent FORTRAN statements using a hypermatrix formulational structure [20]. The operation basic to the finite element algorithm equation 39 is integration of products of the elements of the cardinal basis $\{N_1(x_\ell)\}$, and the associated (gradient) derivative $\frac{\partial}{\partial x_\ell}\{N_1(x_\ell)\}$, for the discretization of R^2 formed by the union of triangles. The master element is graphed in Figure A.1, which illustrates the various required coordinate systems including the linearly dependent natural coordinate system ζ_i. The elements of $\{N_1\}$ are identical to ζ_i, and for any domain R^2_e

$$\int_{R^2_e} \zeta_1^p \, \zeta_2^q \, \zeta_3^r \, d\vec{x} = \frac{A_e}{2} \frac{p!\, q!\, r!}{(2 + p + q + r)!} \tag{A.1}$$

where A_e is the plane area of R^2_e. Furthermore,

$$\{\zeta\} = \left\{ \begin{array}{r} 1 - \bar{\eta}_1/\bar{\eta}_1^2 - (1 - \bar{\eta}_1^3/\bar{\eta}_1^2)\bar{\eta}_2/\bar{\eta}_2^3 \\ \\ \bar{\eta}_1/\bar{\eta}_1^2 - (\bar{\eta}_1^3/\bar{\eta}_1^2)\bar{\eta}_2/\bar{\eta}_2^3 \\ \\ \bar{\eta}_2/\bar{\eta}_2^3 \end{array} \right\} \tag{A.2}$$

and $\bar{\eta}_\ell^\alpha$ denotes the $\bar{\eta}_\ell$ coordinate of node point α, for the sequencing defined in Figure A.1. The elementary transformation defining $\bar{\eta}_\ell = \bar{\eta}_\ell(\eta_k)$ is,

$$\bar{\eta}_\ell = a_{\ell k} \, \eta_k \tag{A.3}$$

where $a_{\ell k}$ are the direction cosines defining $\bar{\eta}_1$ as the line connecting nodes 1 and 2 of R^2. The derivatives of the elements of $\{N_1(\zeta)\}$ are formed, using the chain rule and tensor index summation convention, as

$$\frac{\partial}{\partial x_\ell}\{N_1(\zeta)\} = \frac{\partial}{\partial \zeta_i}\left\{\zeta\right\} \frac{\partial \zeta_i}{\partial \bar{\eta}_j} \frac{\partial \bar{\eta}_j}{\partial \eta_k} \frac{\partial \eta_k}{\partial x_\ell} \tag{A.4}$$

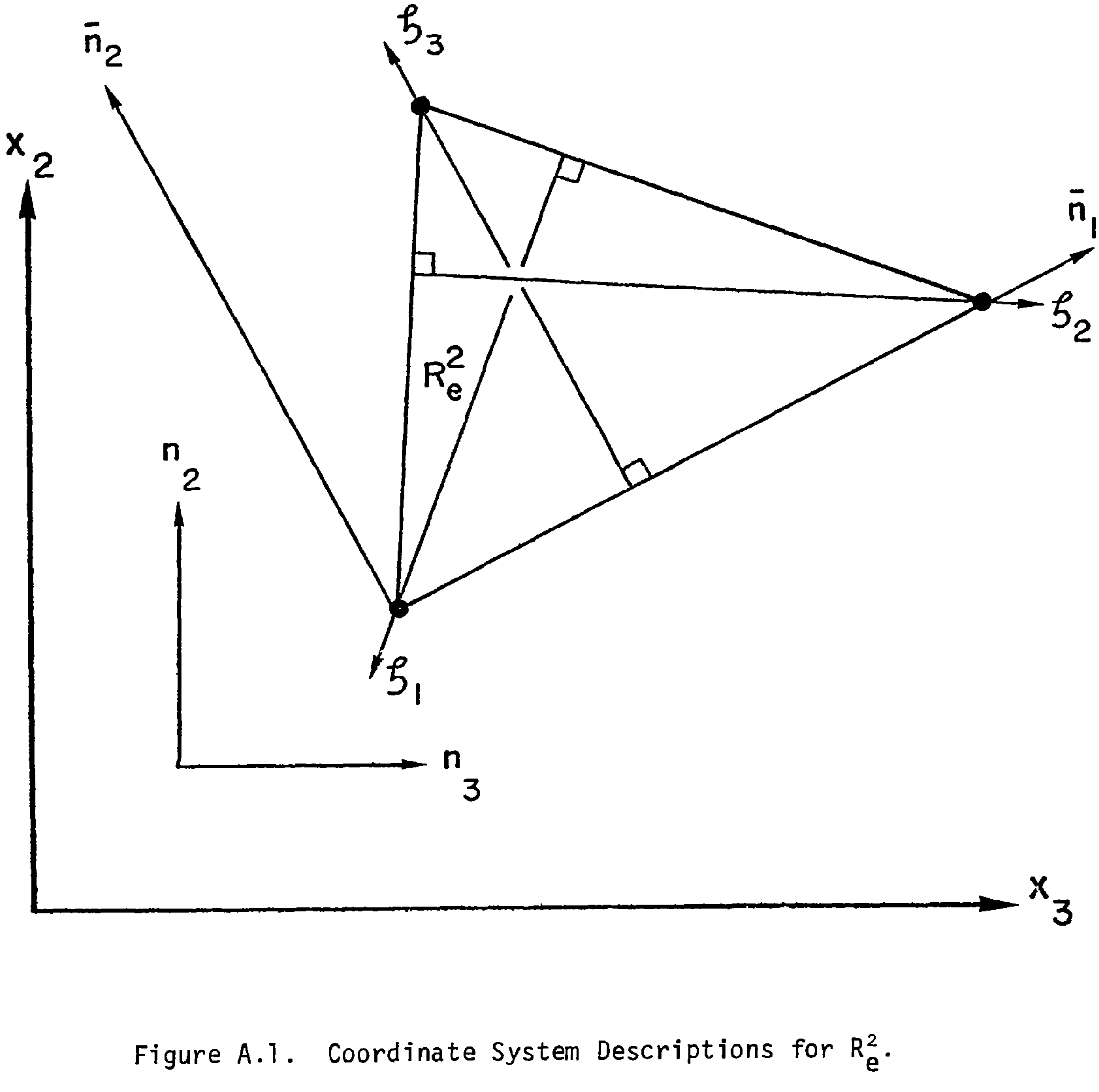

Figure A.1. Coordinate System Descriptions for R_e^2.

Consider the first term of the 3DPNS generalized differential equation whereby the elements of $q_j(x_i) = \{\tilde{u}_1, \tilde{u}_2, \tilde{u}_3, \tilde{H}, k, \varepsilon\}$ are marched in the chordwise (x_1) direction. For the grid-stretching coordinate transformation, equation 31, and subtracting out the continuity equation 1, which yields the "nonconservative form", this term becomes

$$\bar{\rho}\tilde{u}_1\frac{\partial q_j}{\partial x_1} = \bar{\rho}\tilde{u}_1\left[\frac{\partial}{\partial \eta_1} - (h_{22} + \eta_2 h_{23})\frac{\partial}{\partial \eta_2} + (h_{23} + \eta_3 h_{33})\frac{\partial}{\partial \eta_3}\right]q_j \qquad (A.5)$$

Employing the finite element construction equation to interpolate $\bar{\rho}\tilde{u}_1$ and $\eta_\ell(\zeta)$ on R^2_e, yields

$$(\bar{\rho}\tilde{u}_1)^h \equiv \sum_e \{N_1(\zeta)\}^T\{\text{RHOU1}\}_e \qquad (A.6)$$

$$\eta^h_\ell \equiv \sum_e \{N_1(\zeta)\}^T\{\text{ETAL}\}_e \qquad (A.7)$$

The elements of $\{\text{RHOU1}\}_e$ and $\{\text{ETAL}\}_e$ are the nodal values of $\bar{\rho}\tilde{u}_1$ and η_ℓ. Then, the term corresponding to equation A.5 within the error extremization weighted residuals statement, equation 39, upon rearrangement of selected scalars, becomes

$$\int_{R^2}\{N_1\}L(q^h_j)d\tau = \int_{R^2}\{N_1\}\left(\bar{\rho}\tilde{u}^h_1\frac{\partial q^h_j}{\partial x_1}\right)d\vec{x} = S_e\left\{\{\text{RHOU1}\}^T_e\int_{R^2_e}\{N_1\}\{N_1\}\left[\{N\}^T\{QJ\}_e\right.\right.$$

$$\left.\left.-\left(h_{22} + h_{23}\{N_1\}^T\{\text{ETA2}\}_e\right)\frac{\partial\{N_1\}^T}{\partial \eta_2} - (h_{32} + h_{33}\{N_1\}^T\{\text{ETA3}\}_e)\frac{\partial\{N_1\}^T}{\partial \eta_3}\right]d\vec{\eta}\{QJ\}_e\right\} \qquad (A.8)$$

Equation A.8 defines the global calculus operations on $R^2 = \cup R^2_e$, as the matrix assembly (S_e) of the equivalent calculations performed on the master element. (Baker [20, Ch.2] discusses this topic in depth, and rigorously derives the matrix row summation procedures on R^n_e which constitute "assembly".) Note also that the element matrices $\{\text{RHOU1}(x_1)\}_e$ and $\{QJ(x_1)\}_e$ are independent of η_k, and can be extracted outside the integral as shown.

Considering the first term in equation **A.8**, and expanding in terms of $\{\zeta\}$ yields

$$\{\mathrm{RHOU1}\}_e^T \int_{R_e^2} \{N_1\}\{N_1\}\{N_1\}^T d\vec{\eta}\ \{\mathrm{QJ}\}_e$$

$$= \{\mathrm{RHOU1}\}_e^T \int_{R^2} \begin{Bmatrix} \zeta_1 \\ \zeta_2 \\ \zeta_3 \end{Bmatrix} \begin{bmatrix} \zeta_1^2 & \zeta_1\zeta_2 & \zeta_1\zeta_3 \\ & \zeta_2^2 & \zeta_2\zeta_3 \\ (\mathrm{sym}) & & \zeta_2^2 \end{bmatrix} d\vec{\eta}\ \{\mathrm{QJ}\}_e \qquad (\mathrm{A.9})$$

Recalling the matrix rules of scalar multiplication, the column matrix premultiplier in equation A.9 can be brought inside by multiplying every element of $[\cdot]$ by $\{\cdot\}$. This yields a 3 x 3 square matrix, every element of which is a 3 x 1 column matrix, i.e., a "hypermatrix" of degree one. The defined integrals of products of $\zeta_i, 1 \leq i \leq 3$, are easy to evaluate using equation A.1, which yields the finite element matrix equivalent of equation A.9 as

$$\{\mathrm{RHOU1}\}_e^T \int_{R_e^2} \{N_1\}\{N_1\}\{N_1\}^T d\vec{\eta}\{\mathrm{QJ}\}_e = \frac{A_e}{60}\{\mathrm{RHOU1}\}_e^T \begin{bmatrix} \begin{Bmatrix} 6 \\ 2 \\ 2 \end{Bmatrix} & \begin{Bmatrix} 2 \\ 2 \\ 1 \end{Bmatrix} & \begin{Bmatrix} 2 \\ 1 \\ 2 \end{Bmatrix} \\ & \begin{Bmatrix} 2 \\ 6 \\ 2 \end{Bmatrix} & \begin{Bmatrix} 1 \\ 2 \\ 2 \end{Bmatrix} \\ (\mathrm{sym}) & & \begin{Bmatrix} 2 \\ 2 \\ 6 \end{Bmatrix} \end{bmatrix} \{\mathrm{QJ}\}_e'$$

$$\equiv A_e\{\mathrm{RHOU1}\}_e^T[\mathrm{B3000}]\{\mathrm{QJ}\}_e' \qquad (\mathrm{A.10})$$

In equation A.10, A_e is the element plane area, and 1/60 is the normalizing coefficient of the integers constituting the "standard" master hyper-matrix $[\mathrm{B3000}]$. This lexicographic symbol indicates the master matrix is defined on a two-dimensional element (B), and is constituted of the product of three cardinal basis (3), none of which are differentiated (000). If a basis other than $\{N_1(\zeta)\}$ were chosen, the specific entries in $[\mathrm{B3000}]$ would change, of course, but the symbolic representation in the final line of equation A.10 remains unaltered. Matrix multiplications must clear the hyper-matrix rank first; thereafter, the regular rules of matrix algebra apply.

Returning to equation A.8, the grid stretching coordinate transformation has introduced additional terms which involve derivatives of elements of $\{N_1(\zeta)\}$ on the η_k. Using equation A.4,

$$\frac{\partial}{\partial\eta_\ell}\{N_1(\zeta)\} = h_{21}(x_1)\{B112\}_e\,\hat{e}_2 + h_{31}(x_1)\{B113\}_e\,\hat{e}_3 \tag{A.11}$$

The elements of $\{B11K\}_e$, which are element-dependent, 3 x 1 column matrices, are strictly a function of the node coordinates $\bar{\eta}_\ell^\alpha$ of R_e^2 , see equation A.2, and the set $a_{\ell k}$ of direction cosines, equation A.3. The unit vectors $\hat{e}_k$ are parallel to the x_ℓ coordinate system, and the metrics h_{k1} are functions of x_1 at most. Therefore, equation A.11 is the matrix equivalent of the directional derivative with scalar components parallel to $\tilde{u}_\ell$. Then, on the master element, the second and third terms in equation A.8 are of the form

$$\{RHOU1\}_e^T\int\{N_1\}\{N_1\}\left(-h_{\ell 2} - h_{\ell 3}\ \{N_1\}^T\{ETAL\}_e\right)\frac{\partial\{N_1\}^T}{\partial\eta_\ell}\,d\vec{\eta}\ \{QJ\}_e$$

$$= A_e\{RHOU1\}_e^T\Bigg[\Big[-h_{22}\ h_{21}[B200] - h_{23}\ h_{21}[B3000]\{ETA2\}_e\Big]\{B112\}_e^T\{QJ\}_e$$

$$+ \Big[-h_{32}\ h_{31}[B200] - h_{33}\ h_{31}[B3000]\{ETA2\}_e\Big]\{B113\}_e^T\{QJ\}_e\Bigg] \tag{A.12}$$

The master hyper-matrix [B3000] was defined in equation A.10; it is an elementary operation to further show that

$$[B200] = \frac{1}{12}\begin{bmatrix} 2 & 1 & 1 \\ & 2 & 1 \\ (\text{sym}) & & 2 \end{bmatrix} \tag{A.13}$$

In distinction to the comments regarding the universality of the symbol [B3000] for all (k^{th} degree) cardinal basis specifications $\{N_k\}$, the form of equation A.13 would change if the elements of $\frac{\partial}{\partial \eta_\ell}\{N_k\}$ are functions of η_ℓ. The general statement for equation A.8 is,

$$\int_{R_e^2} \{N_k\}\left(\bar{\rho}\tilde{u}_1^h \frac{\partial q_j^h}{\partial x_1}\right) d\vec{x} = A_e \{RHOU1\}_e^T [B3000]\{QJ\}'_{\theta}$$

$$+ A_e \{RHOU1\}_e^T \Big[-h_{\ell 2} h_{\ell 1} [B300L]_e - h_{\ell 3} h_{\ell 1} [B400LO]_e \{ETAL\}_e\Big] \{QJ\}_e \qquad (A.14)$$

In equation A.14, the index $\ell(L)$ is a tensor index that takes the values $2 \le (\ell, L) \le 3$. Furthermore, [B400LO] is a hypermatrix of degree two; the first and last Boolean indices (0) indicate $\{RHOU1\}_e$ and $\{ETAL\}_e$ are interpolated, and these (inner) multiplications must be performed prior to post-multiplication by $\{QJ\}_e$, which has been differentiated parallel to $\eta_\ell(L)$. The remaining terms in the finite element algorithm statement, equation 39, are formed in the same manner

The second major formulational step is construction of the Jacobian of the Newton iteration algorithm, equation 42. By definition,

$$[J] \equiv \frac{\partial \{FJ\}}{\partial \{QI\}} \qquad (A.15)$$

with {FJ} given by equation 41. Continuing with the example of the downstream convection term, the specific form for the resultant expressions in {FJ} is

$$\{FJ\} = S_e \Bigg(A_e \{\overline{RHOU1}\}_e^T [B3000] \left(\{QJ\}_{j+1}^p - \{QJ\}_j\right)$$

$$- \frac{\Delta x_1}{2} \Bigg[A_e \{\overline{RHOU1}\}_e^T \Big[h_{\ell 2} h_{\ell 1} [B300L]_e$$

$$+ h_{\ell 3} h_{\ell 1} [B400LO]_e \{ETAL\}_e \Big] \{QJ\} + \cdots \Bigg]_{j+1,j} \Bigg) \qquad (A.16)$$

In equation A.16, $\{\overline{RHOU1}\}_e \equiv \frac{1}{2}(\{RHOU1\}^p_{j+1} + \{RHOU1\}_j)$, and $\Delta x_1 = x_{j+1} - x_j$, is the chordwise marching step-size. Furthermore, $\cdot]_{J+1,j}$ indicates the algebraic average, and superscript p is the iteration index, see equation 43. For equation A.15, the independent variable is $\{QJ\}^p_{j+1}$; therefore, the elemental contributions to [J] become formed as

$$\frac{\partial\{FJ\}_e}{\partial\{QI\}_e} = A_e\{\overline{RHOU1}\}^T_e[B3000]\delta_{JI} - \frac{\Delta x_1 A_e}{2}\{RHOU1\}^T_e\Big[h_{\ell 2}h_{\ell 1}[B300L]_e + h_{\ell 3}h_{\ell 1}[B400L0]\{ETAL\}_e\Big]\delta_{JI} + \frac{\partial\{FJ\}}{\partial\{RHOU1\}}\,\frac{\partial\{RHOU1\}}{\partial\{QI\}} \tag{A.17}$$

In equation A.17, δ_{JI} is the discrete index Kronecker delta, which yields the self-dependence expressions, i.e., $\partial\{FJ\}/\partial\{QJ\}$. Since $\bar{\rho}\tilde{u}_1^h$, i.e., $\{\overline{RHOU1}\}$, is a function of both $\bar{\rho}$ and $\tilde{u}_1$, which are dependent variables, the second term in equation A.17 yields the nonself coupling. The algebraic equation of state yields $\bar{\rho} = \bar{\rho}(p,\tilde{H})$; for subsonic flows, the density variation is very weak and therefore can be neglected in [J]. Using the chain rule, then

$$\frac{\partial\bar{\rho}\tilde{u}_1^h}{\partial q_i^h} \approx \bar{\rho}\delta_{1i} \tag{A.18}$$

Hence, interchanging orientation in the hypermatrix formations, as required, yields

$$\frac{\partial\{FJ\}}{\partial\{\overline{RHOU1}\}}\,\frac{\partial\{\overline{RHOU1}\}}{\partial\{QI\}} = \frac{A_e\bar{\rho}_e}{2}\{QI\}^T_e[B3000]\delta_{J1}\delta_{I1} - \frac{\Delta x_1 A_e\bar{\rho}_e}{4}\{QI\}^T_e\Big[h_{\ell 2}h_{\ell 1}[B3000] + h_{\ell 3}h_{\ell 1}[B4L000]\{ETAL\}_e\Big]\delta_{J1}\delta_{I1} \tag{A.19}$$

In equation A.19, $\bar{\rho}_e$ is the element-average value of $\bar{\rho}$ on R_e^2. The CMC:3DPNS computer code neglects all nonself coupling in construction of the Jacobian $[J]$. Therefore, $[J]$ is independent of the specific element of $q_j^h = \{\tilde{u}_1, \tilde{u}_2, \tilde{u}_3, H, k, \varepsilon\}$. Hence, the single LU decomposition of $[J(QJ)]_{j+1}^p$ is employed to solve for the appropriate six elements of $\{\delta Q\}_{j+1}^{p+1}$, using a multiple right-hand side procedure in equation 42. The Jacobian is updated for each iteration within step Δx_{j+1}.

Equations A.14, A.17 and A.19 are illustrative of the operational procedures of formulation of the finite element algorithm statement for aerodynamic juncture region flow. There is an exacting amount of detail required to complete all aspects of the 3DPNS algorithm statement. However, the developed hypermatrix formalisms and master element concepts have produced a rigorous procedure to keep track of the details. The role of the tensor indices and matrix differential calculus are invaluable tools put to practical use. Finally, note that these equations are written in a pseudo-FORTRAN language which yields coding which is nominally identical in appearance to the theoretical statements.

REFERENCES

1. Rubin, S. G., "Incompressible Flow Along a Corner," J. Flu. Mech., V. 26, Pt. 1, 1966, pp. 97-110.

2. Pal, A., and Rubin, S. G., "Asymptotic Features of Viscous Flow Along a Corner," J. Q. Appl. Math., V. 27, 1971, pp. 99-108.

3. Rubin, S. G., and Grossman, B., "Viscous Flow Along the Corner: Numerical Solution of the Corner Layer Equations," J. Q. Appl. Math., V. 29, No. 2, 1971, pp. 169-186.

4. Weinberg, B. C., and Rubin, S. G., "Compressible Corner Flow," J. Flu. Mech., V. 56, Pt. 4, 1972, pp. 753-774

5. Tokuda, N., "Viscous Flow Near a Corner in Three Dimensions," J. Flu. Mech., V. 53, Pt. 1, 1972, pp. 129-148.

6. Zamir, M., and Young, A. D., "Experimental Investigation of the Boundary Layer in a Streamwise Corner," J. Aero. Qtly., V. 21, 1970, pp. 313-339.

7. Bragg, G. M., "The Turbulent Boundary Layer in a Corner," J. Flu. Mech., V. 36, Pt. 3, 1969, pp. 485-503.

8. Eichelbrenner, E. A., and Preston, J. H., "On a Role of Secondary Flow in Turbulent Boundary Layers in Corners (and salients)," J. deMecanique, V. 10, No. 1, 1971, pp. 91-112.

9. Gessner, F. B., "The Origin of Secondary Flow in Turbulent Flow Along a Corner," J. Flu. Mech., V. 58, Pt. 1, 1973, pp. 1-25.

10. Gessner, F. B., and Emery, A. F., "A Reynolds Stress Model for Turbulent Corner Flows - Pt. I: Development of the Model,: J. Flu. Engr., Trans. ASME, 1976, pp. 261-268.

11. Melling, A., and Whitelaw, J. H., "Turbulent Flow in a Rectangular Duct," J. Fluid Mech., V. 78, Pt. 2, 1976, pp. 289-315.

12. Shabaka, I.M.M.A., and Bradshaw, P., "Turbulent Flow Measurement in an Idealized Wing/Body Juncture," AIAA J., V. 19, No. 2, 1981, pp. 131-132.

13. McMahon, H., Hubbartt, J. and Kubendran, L., "Mean Velocities and Reynolds Stresses in a Juncture Flow." NASA CR - 3605, 1982.

14. Briley, W. R., and McDonald, H., "Analysis and Computation of Viscous Subsonic Primary and Secondary Flows," Technical Paper AIAA-79-1453, 1979.

15. Oden, J. T., "A Theory of Penalty Methods for Finite Element Approximations of Highly Nonlinear Problems in Continuum Mechanics," Comp. & Structures, V. 8, 1978, pp. 445-449.

16. Cebeci, T., and Smith, A.M.O., Analysis of Turbulent Boundary Layers, Academic Press, New York, 1974.

17. Launder, B. E., Reece, G. J., and Rodi, W., "Progress in the Development of a Reynolds-Stress Turbulence Closure," J. Flu. Mech., V. 68, Pt. 3, 1975, pp. 537-566.

18. Hanjalic, K., and Launder, B. E., "A Reynolds Stress Model of Turbulence and its Application to Thin Shear Flows," J. Flu. Mech., V. 52, Pt. 4, 1972, pp. 609-638.

19. Lumley, J. L., "Toward a Turbulent Constitutive Relation," J. Flu. Mech., V. 41, Pt. 2, 1970, pp. 413-434.

20. Baker, A. J., Finite Element Computational Fluid Mechanics, McGraw-Hill/Hemisphere, New York, 1983.

21. Pratrap, V. S., and Spalding, D. B., "Numerical Computations of the Flow in Curved Ducts," J. Aero. Qtrly, V. 26, 1975.

22. Rodi, W., "Progress in Turbulence Modeling for Incompressible Flows," Technical Paper AIAA-81-0045, 1981.

23. Baker, A. J., Yu, J. C., Orzechowski, J. A., and Gatski, T. B., Prediction and Measurement of Incompressible Turbulent Aerodynamic Trailing Edge Flows," AIAA J., V. 20, No. 1, 1982, pp. 51-59.

24. Baker, A. J., and Orzechowski, J. A., "An Interaction Algorithm for Prediction of Mean and Fluctuating Velocities in Two-Dimensional Aerodynamic Wake Flows." NASA CR-3301, 1980.

25. Prenter, P. M., Splines and Variational Methods, Wiley-Interscience, New York, 1975.

26. Oden, J. T., and Reddy, J. N., An Introduction to the Mathematical Theory of Finite Elements, Wiley-Interscience, New York, 1976.

27. Strang, G., and Fix, G. J., An Analysis of the Finite Element Method, Prentice-Hall, New Jersey, 1973.

28. Soliman, M. O., and Baker, A. J., "Accuracy and Convergence of a Finite Element Algorithm for Laminar Boundary Layer Flow," J. Comp. Flu., V. 9, 1981, pp. 43-62.

29. Soliman, M. O., and Baker, A. J., "Accuracy and Convergence of a Finite Element Algorithm for Turbulent Boundary Layer Flow," J. Comp. Mtd. App. Mech. and Engr., V. 28, 1981, pp. 81-102.

30. Hess, J. L., "Calculation of Potential Flow About Arbitrary Three-Dimensional Lifting Bodies," Rep. No. MDC J5679-01 (Contract N00019-71-C-0524), McDonnell Douglas Corp., Oct. 1972. (Available From DTIC as AD 755 480.)

31. Shafir, M., and Rubin, S. G., "The Turbulent Boundary Layer Near a Corner," Technical Paper ASME-76-APM-PP, J. Appl. Mech., 1976.

32. Baker, A. J., and Orzechowski, J. A., "A Continuity-Constraint Finite Element Algorithm for Three-Dimensional Parabolic Flow Prediction," in Computers in Flow Predictions and Fluid Dynamics Experiments, ASME, New York, 1981, pp. 103-117.

1. Report No. NASA CR-3645	2. Government Accession No.	3. Recipient's Catalog No.

4. Title and Subtitle
THE CMC:3DPNS COMPUTER PROGRAM FOR PREDICTION OF THREE-DIMENSIONAL, SUBSONIC, TURBULENT AERODYNAMIC JUNCTURE REGION FLOW. VOLUME I - THEORETICAL

5. Report Date
November 1982

6. Performing Organization Code

7. Author(s)
A. J. Baker

8. Performing Organization Report No.
COMCO:81TR-2.1

9. Performing Organization Name and Address
Computational Mechanics Consultants, Inc.
3601A Chapman Highway
Knoxville, Tennessee 37920

10. Work Unit No.

11. Contract or Grant No.
NAS1-15105/MOD. 5

12. Sponsoring Agency Name and Address
National Aeronautics and Space Administration
Washington, D.C. 20546

13. Type of Report and Period Covered
Contractor Report

14. Sponsoring Agency Code

15. Supplementary Notes
Langley Technical Monitor: Douglas L. Dwoyer

16. Abstract

An order-of-magnitude analysis of the subsonic three-dimensional steady time-averaged Navier-Stokes equations, for semi-bounded aerodynamic juncture geometries, yields the parabolic Navier-Stokes simplification. The numerical solution of the resultant pressure Poisson equation is cast into complementary and particular parts, yielding an iterative interaction algorithm with an exterior three-dimensional potential flow solution.

A parabolic transverse momentum equation set is constructed, wherein robust enforcement of first-order continuity effects is accomplished using a penalty differential constraint concept within a finite element solution algorithm. A Reynolds stress constitutive equation, with low turbulence Reynolds number wall functions, is employed for closure, using parabolic forms of the two-equation turbulent kinetic energy-dissipation equation system. Numerical results document accuracy, convergence and utility of the developed finite element algorithm, and the CMC:3DPNS computer code applied to an idealized wing-body juncture region. Additional results document accuracy aspects of the algorithm turbulence closure model.

17. Key Words (Suggested by Author(s))	18. Distribution Statement
Parabolic Navier-Stokes Finite Element Algorithm Three-Dimensional, Subsonic Turbulent	Unclassified - Unlimited Subject Category 34

19. Security Classif. (of this report)	20. Security Classif. (of this page)	21. No. of Pages	22. Price
Unclassified	Unclassified	60	A04

For sale by the National Technical Information Service, Springfield, Virginia 22161

NASA-Langley, 1982